The FEBS Journal

FEBS PRESS science publishing by scientists

Salmonella-driven intestinal edema in mice is characterized by tensed fibronectin fibers

Ronja Rappold[1,2], Konstantinos Kalogeropoulos[3], Ulrich auf dem Keller[3,†], Viola Vogel[1,4] and Emma Slack[2,4]

1 Institute of Translational Medicine, ETH Zurich, Switzerland
2 Institute of Food, Nutrition and Health, ETH Zurich, Switzerland
3 Department of Biotechnology and Biomedicine, Technical University of Denmark, Kgs. Lyngby, Denmark
4 Botnar Research Center for Child Health, Basel, Switzerland

Keywords
extracellular remodeling; fibronectin; intestinal edema; laser capture microdissection; LC–MS/MS proteomics

Correspondence
E. Slack and V. Vogel, Department of Health Sciences and Technology, ETH Zurich, 8093 Zurich, Switzerland
Tel: +41 44 632 45 91; +41 44 632 08 87
E-mail: emma.slack@hest.ethz.ch; viola.vogel@hest.ethz.ch

Emma Slack and Viola Vogel share senior authorship
†Deceased

(Received 24 August 2023, revised 4 December 2023, accepted 5 March 2024)

doi:10.1111/febs.17120

Intestinal edema is a common manifestation of numerous gastrointestinal diseases and is characterized by the accumulation of fluid in the interstitial space of the intestinal wall. Technical advances in laser capture microdissection and low-biomass proteomics now allow us to specifically characterize the intestinal edema proteome. Using advanced proteomics, we identify peptides derived from antimicrobial factors with high signal intensity, but also highlight major contributions from the blood clotting system, extracellular matrix (ECM) and protease–protease inhibitor networks. The ECM is a complex fibrillar network of macromolecules that provides structural and mechanical support to the intestinal tissue. One abundant component of the ECM observed in *Salmonella*-driven intestinal edema is the glycoprotein fibronectin, recognized for its structure–function interplay regulated by mechanical forces. Using mechanosensitive staining of fibronectin fibers reveals that they are tensed in the edema, despite the high abundance of proteases able to cleave fibronectin. In contrast, fibronectin fibers increasingly relax in other cecal tissue areas as the infection progresses. Co-staining for fibrin(ogen) indicates the formation of a provisional matrix in the edema, similar to what is observed in response to skin injury, while collagen staining reveals a sparse and disrupted collagen fiber network. These observations plus the absence of low tensional fibronectin fibers and the additional finding of a high number of protease inhibitors in the edema proteome could indicate a critical role of stretched fibronectin fibers in maintaining tissue integrity in the severely inflamed cecum. Understanding these processes may also provide valuable functional diagnostic markers of intestinal disease progression in the future.

Introduction

The function of the gastrointestinal tract is to digest and absorb nutrients from food into the mammalian body, while maintaining the physical as well as immunological barrier against harmful substances and pathogens from outside. During an invasive enterobacterial infection, local and systemic inflammatory reactions act to limit the size of the invaded pathogen population and to prevent its spread to systemic sites. Intestinal edema is

Abbreviations
Capn, calpain; CHP, collagen hybridizing peptide; Cst3, cystatin-C; ECM, extracellular matrix; GO, Gene Ontology; H&E, hematoxylin & eosin; LCN2, lipocalin-2; Lgmn, legumain; MMP, matrix metalloprotease; p.i., postinfection; PBS, phosphate-buffered saline; *S.* Tm, *Salmonella enterica* subspecies *enterica* serovar Typhimurium; serpin, serine proteinase inhibitor.

caused by the build-up of excess fluid in the interstitial spaces of the intestinal wall. Edema formation together with immune cell infiltration and ulceration of the epithelial layer are common pathological observations in intestinal diseases [1]. Abnormal fluid accumulation in the interstitium of the intestinal wall tissue leads to swelling and physical separation of the two smooth muscle layers present in the cecum. Intestinal edema formation is typically thought of as detrimental to tissue homeostasis due to the impairment of the organ's mechanical and physiological functions. The diffusion distance of oxygen and other nutrients is dramatically increased, while the transport of toxic byproducts is impeded [2]. Furthermore, it was reported that edema can lead to a decrease in smooth muscle cell contraction in the intestine, limiting bowel movement in the already challenged inflamed organ [3,4]. Conversely, edema represents a useful response to intestinal infection as tissue swelling reduces the gut luminal volume, limiting the colonizable space, and therefore the total population size, for pathogens such as *Salmonella* Typhimurium. Non-typhoidal *Salmonella* infections are still one of the most common causes of diarrheal diseases and represent a major public health concern with several tens of million cases of gastroenteritis globally each year [5–7]. One of the most important subspecies is *Salmonella enterica* subspecies *enterica* serovar Typhimurium (*S.* Tm), causing gastroenteritis in humans and animals. *S.* Tm infection mechanisms have been widely studied [8,9] using germ-free or antibiotics pre-treated specific pathogen-free mice [10,11]. After oral infection, *S.* Tm passes through the gastrointestinal tract and reaches the large intestine, its major site of replication in the mouse intestine [12]. Tissue invasion by the bacteria induces a multitude of host defense mechanisms: secretion of antimicrobial peptides, recruitment of neutrophils and other inflammatory cell types, expulsion of infected epithelial cells as well as production of pathogen-specific IgA to clear bacteria from the lumen [13–16]. These host reactions limit systemic spread of *Salmonella* [8], but also cause collateral damage to the commensal microbiota and damage to intestinal tissues [17,18].

The extracellular matrix (ECM), the complex network of proteins and carbohydrates providing structural integrity to cells and tissues, is now considered to play an important role in controlling interstitial volume [19]. However, it is still unclear how exactly the ECM contributes or counteracts potential tissue swelling. The main ECM components include collagens, glycoproteins such as fibronectin, and carbohydrates such as glycosaminoglycans, and various ECM-associated growth factors [20,21]. In particular, fibronectin's important role in tissue growth and wound healing has been extensively studied [22–24]. Fibronectin knock-out mice do not survive past early stages of development and the embryos start to deteriorate after embryonic day 8 [25]. This lethality demonstrates the vital role that fibronectin plays in the overall development and survival of animals and limits animal studies to active measurement and observation. Fibronectin fibers as well as a variety of other ECM fibers can be mechanically stretched and partially unfolded, entailing functional consequences such as altered growth factor or cytokine binding, altered enzymatic fiber cleavage or accessibility of binding sites [26]. Fibronectin fiber stretching can also activate cryptic binding sites, which are not accessible in the equilibrated fibronectin molecule and are important for, but not limited to, fibronectin matrix assembly [22,26]. Additionally, interleukin-7 [27] and tissue transglutaminase [28] binding have been reported to be dependent on the tensile state of fibronectin fibers, as well as the templating of collagen on fibronectin fibers, which is required to initiate the onset of collagen I fibrillogenesis [29]. These effects in turn were also shown to affect cellular signaling and behavior *in vitro* [30,31]. Despite the importance of fibronectin fibers already demonstrated in other model systems, if and how these fibers are involved in the build-up or resolving phase of intestinal edema remains to be investigated.

To confirm that cell generated forces are sufficient to stretch fibronectin fibers and induce fibronectin's partial unfolding in cell culture, an *in vitro* fibronectin tension probe was already developed more than 20 years ago, labeled with donors and acceptors for fluorescence resonance energy transfer measurements [32]. Probing the tensional state of tissue fibers in organs, however, is much more challenging [26]. The Vogel lab developed a peptide probe, making use of adhesin fragments, specifically FnBPA5 of *Staphylococcus aureus*, that were evolutionary optimized by the bacteria to recognize mechanically or enzymatically cleaved fibers, for example as found in complex biological wound settings [33,34]. FnBPA5 binds with nanomolar affinity to the N-terminal fibronectin domains $FnI_{2–5}$, but only if the fibers are in a low tensional state [35]. This is highly significant as polyclonal antibodies, in contrast, typically bind proteins independent of their tensional state. Stretching of fibronectin fibers destroys the multivalent network of backbone hydrogen bonds formed between FnBPA5 and the four FnI domains [33]. Thus, in stretched fibronectin fibers, the structural match and the affinity between FnI_{2-5} and the FnBPA5 peptide is lost as the interdomain distance between the fibronectin type I modules

is increasing. Coupling of the FnBPA5 peptide to a fluorophore thus allows to specifically detect relaxed fibronectin fibers in *ex vivo* animal tissues [36–38]. Of note, FnBPA5 cannot distinguish between fibronectin fibers that are structurally relaxed due to the presence of other load-bearing ECM fibers, such as collagen fibers [29], or due to fibronectin fiber cleavage since both processes increase the multivalent binding of FnBPA5 to sequential type I domains. The herein applied FnBPA5 probe is, to the best of our knowledge, the only broadly validated tool available for *ex vivo* investigations of fibronectin fiber tension. It shows very good tissue penetration qualities, has a characterized binding motif as well as binding affinity, and was extensively characterized and validated in multiple studies at the molecular [33,35], cell, and tissue level [36–38].

Studying edema composition is technically challenging as there are few cells, rendering spatial transcriptomics uninformative. There are no known specific reporter or cell-type-specific knock-out systems for interventional mechanistic studies, necessarily limiting us to detailed observation. Additionally, the contribution of these fluid-filled areas to the total tissue proteome is minimal, such that standard proteomics approaches fail to represent the edema content. Recent advances in microscopy, laser capture microdissection and proteomics on very-low-biomass samples now make this possible. In this *in vivo* study, we explored the biochemical changes occurring during *Salmonella*-driven edema formation and investigated how fibronectin fiber stretching changes during the tissue remodeling process, utilizing the FnBPA5 fibronectin fiber tension probe that binds only to low tension, but not to high tension fibronectin fibers [33,35–38]. Unbiased discovery proteomics of dissected edema tissue for the first time revealed the protein composition of intestinal edema, and uncovered the major role of the blood clotting system and extracellular matrix within these sites. With this distinct characterization of the edema-specific proteome, we set the foundation for future work on understanding the impact of edema components on cecal inflammation as well as intestinal tissue healing in case of disease survival.

Results

The streptomycin mouse model for non-typhoidal *Salmonella* infection is a widely used and highly reproducible model of gastrointestinal inflammation, inducing clinical and histological features of typhlocolitis. The transient clearance of the gut microbiota by orally administered antibiotics opens a metabolic niche for *Salmonella* in the upper large intestine, allowing *S.* Tm to colonize at densities exceeding 10^9 colony forming units (CFU) per gram of gut content. The pathological tissue changes of the disease include neutrophil infiltration, submucosal edema, goblet cell depletion and epithelial disruption. Of these phenomena, the induction and control of submucosal edema is the least well-understood. We therefore first characterized the histopathological and mechanobiological changes in *S.* Tm-infected cecal tissue to gain insight into potential mechano-regulatory pathways involved in this process.

Twenty-five wild-type specific-pathogen-free C57BL/6 mice were fed a high dose of streptomycin the day before infection. Five of the streptomycin-pretreated animals were mock infected and 20 animals were fed 5×10^7 CFU of *S.* Tm, mimicking food-borne infection. The widely used inflammation marker, fecal lipocalin-2 (LCN2), was used to determine the severity of the intestinal inflammation directly from feces samples. Fecal LCN2 levels measured over the disease timecourse confirmed similar disease kinetics in comparison to previously reported infections using oral gavage [10,39,40]. The LCN2 values rapidly increased between 6 h postinfection (p.i.), and 24 h p.i., up to values of 10^3 ng·g^{-1} of feces. Over the next 2 days, the LCN2 levels were further raised to 10^4 ng·g^{-1} of feces at 72 h p.i., indicating severe gastrointestinal inflammation (Fig. 1C).

Cecum size and cross-sectional luminal area significantly decreased during inflammation

Edema development was monitored over the course of the disease at 6, 24, 48 and 72 h p.i.. All dissected cecum organs were first rinsed with phosphate-buffered saline (PBS) to remove existing intestinal content and parts of the mucus layer in order to avoid detachment of the cryosections from the glass during the staining procedure. Subsequently, the rinsed cecum organs were filled with embedding medium for tissues to preserve the original organ appearance. The intrinsic elasticity and stiffness impeded an overstretching of the organ when manually filling it with embedding medium.

Pathohistological assessment using hematoxylin & eosin (H&E) stains clearly showed the kinetics of tissue remodeling (Fig. 1A,B, Fig. S1). The circumference of the tissue decreased significantly during disease progression, supporting the visual impression of the cecum size during the dissection of the mice. On the last day of the infection, the circumference of the cecum had decreased by 25% compared to the control group (Fig. 1D). This observation can be further validated when looking at the luminal diameter change of the cecum tissue. The major inner axis of a fitted ellipse, representing the

diameter of the lumen, decreased from 8 mm in healthy animals to 4 mm in severely inflamed animals (Fig. 2A, B). Furthermore, we analyzed the differences in length between the two muscle layers, muscularis mucosa and muscularis externa from H&E-stained tissue sections as a function of time (Fig. 2C,D). In mock infected mice as well as mice at 6 h p.i., the circumference of the inner and outer muscle layer were almost the same. At 24 h p.i., the length of the muscularis externa decreased by 7.5% averaged over multiple sections from the 5 mice (muscularis mucosa decreased by 3.8%). This effect was more pronounced at 48 h p.i. (muscularis externa further decreased by 21% and muscularis mucosa by 18%) when the muscularis mucosa layer started to take on a buckled morphology. This can be clearly seen visually in the H&E-stained cecum cross-section images at 48 h p.i., showing a buckled mucosa plus muscularis mucosa layer (Fig. 1A,B). Surprisingly, at 72 h p.i., 4 out of 5 animals showed a greatly decreased ratio between the inner and outer muscle layer due to a much stronger decrease in muscularis mucosa length relative to the muscularis externa.

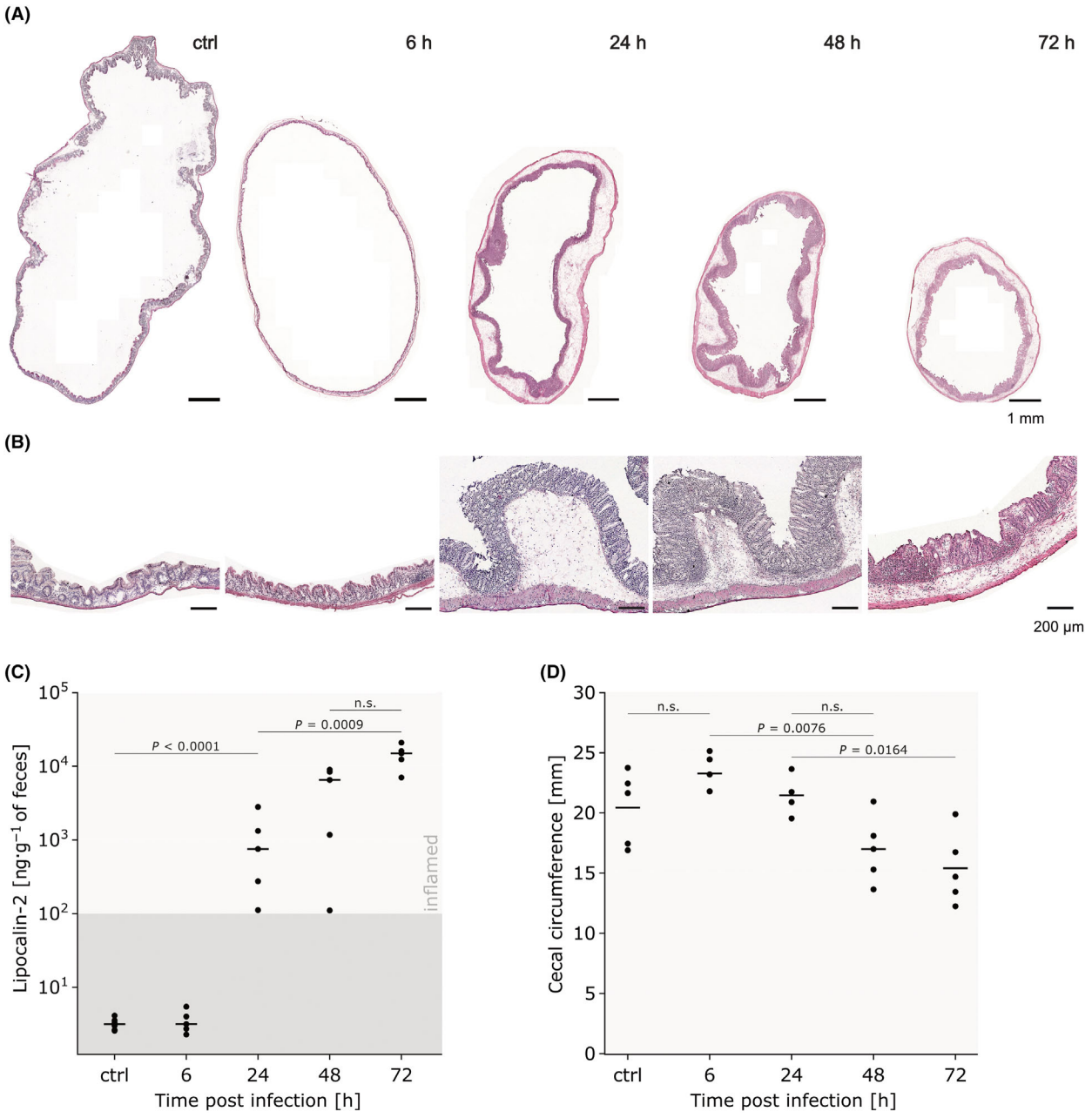

Fig. 1. Histopathological analysis of *S.* Tm-infected cecum in C57BL/6 mice shows decrease in overall cecum size with progressing infection time and inflammation. (A) Representative H&E-stained whole cecum cryosections during the disease timecourse (control mouse, 6, 24, 48 and 72 h postinfection (p.i.)), reveal morphological changes in all cecal tissue layers. H&E-stained sections for all 25 mice in Fig. S1. Scale bar: 1 mm. (B) Higher magnification images of representative parts of H&E-stained cecum sections during the same timeline show pathological tissue changes in more detail. After 24 h p.i. the tissues show a clear inflammatory response including submucosal edema formation, polymorphonuclear granulocyte infiltration as well as epithelial integrity loss. Scale bar: 200 μm. (C) Fecal Lipocalin-2 measurements during the timecourse of the infection confirm the increase in severity of the gastrointestinal inflammation. The dark gray shaded area represents the range of normal values in healthy mice. Marker points represent individual mice ($n = 5$ per group), horizontal lines indicate median of the different groups. Statistical analysis: One-way ANOVA of log-normalized data with Tukey's multiple comparison test, *P*-values indicated, n.s.: $P \geq 0.05$. (D) Quantification of the outer cecal circumference demonstrates a significant decrease over the course of the inflammation. Datapoints represent averaged values for 4–5 individual mice per group, which were calculated from at least 3 H&E-stained cryosections. Horizontal lines indicate the mean value of the different groups. Statistical analysis: One-way ANOVA with Tukey's multiple comparison test, *P*-values indicated, n.s.: $P \geq 0.05$. H&E, hematoxylin & eosin; *S.* Tm, *Salmonella enterica* subspecies *enterica* serovar Typhimurium.

This indicates considerable tissue remodeling during this time window, sufficient to eliminate the buckling formation. The one exceptional mouse that still had a buckled mucosa in the cecal H&E-stained cross-sections and the unaltered muscular ratio, has a lower fecal LCN2 value comparable to the other mice on day 2. This indicates that the inflammation in this mouse is slightly delayed and explains the different morphological appearance.

Specifically focusing on the edema at 6 h, little to no swelling of the submucosa was observable. By the 24 h timepoint, severe edema formation is clearly visible. Surprisingly, we observed a decrease in edema area as fraction of total tissue area over the remaining course of the disease (48 and 72 h p.i.). While we observed large edema throughout the 3-day timecourse, on day 1 of the infection almost 55% of the tissue area was occupied by edema, which decreased to 40% on average on day 3 (Fig. 2E).

Cell numbers and collagen density are significantly reduced in intestinal edema compared to the surrounding tissue layers

Another interesting observation made from the histological assessment was the low number of cells in the submucosal layer in comparison to the mucosa and muscularis externa. In line with expected fluid accumulation, quantification of cell numbers showed an almost 10-fold lower cell number per unit area in the edema in comparison to the mucosal layer (Fig. 3A). In addition, we observed an increase in cell numbers in mucosa and muscularis externa until day 2 postinfection, which is probably caused by infiltration of neutrophils and other proinflammatory immune cells [14]. On day 3, cell numbers dropped in these two tissue layers, likely indicating a terminal loss of tissue integrity. Picrosirius Red staining for collagen proved the high collagen content in mucosa and muscularis externa during the complete timecourse (Fig. 3C). In contrast to the dense collagen network in these adjacent tissue layers, the collagen content in the edema is sparse and quantification of positive picrosirius red-stained pixels yielded a collagen positive pixel density of only 50% compared to the mucosa and muscularis externa (Fig. 3B). The importance of tissue collagen in providing a stable matrix for cells and maintaining tissue integrity is well acknowledged [20,41]. In addition, the picrosirius red-stained cryosections suggest impairment of collagen fiber integrity in the edema (Fig. 3C,D). To investigate this in more detail, a collagen hybridizing peptide (CHP) was used, which binds to denatured collagen helices based on collagen's secondary structure and thus identifies mechanically or biochemically damaged collagen fibers [42,43]. The worm-like appearance of short collagen helix bundles in the picrosirius red stainings was confirmed to be damaged collagen with this CHP binding (Videos S1 and S2). Collagen fibers are less extendable than fibronectin fibers [44] and might get mechanically damaged during submucosal tissue expansion or alternatively get enzymatically cleaved. Z-stacks of CHP-stained as well as fibronectin-stained cryosections displayed a strong difference in how the cells are embedded into the respective fiber networks. While individual cells are found to be embedded in the fibronectin matrix that is tightly intermingled with a fibrin network, collagen fibers seem to be mostly attached to the periphery of cell nests but not to penetrate them (Videos S1–S4). To minimize the impact of tissue sectioning on fiber tension and fragmentation, 20 μm thick cryosections were utilized and our images were taken from inner slices. The reduced collagen density and its disjointed, non-tensed appearance within the edema suggest that collagen fibers are not any longer part of the intact force-bearing, ECM fiber network.

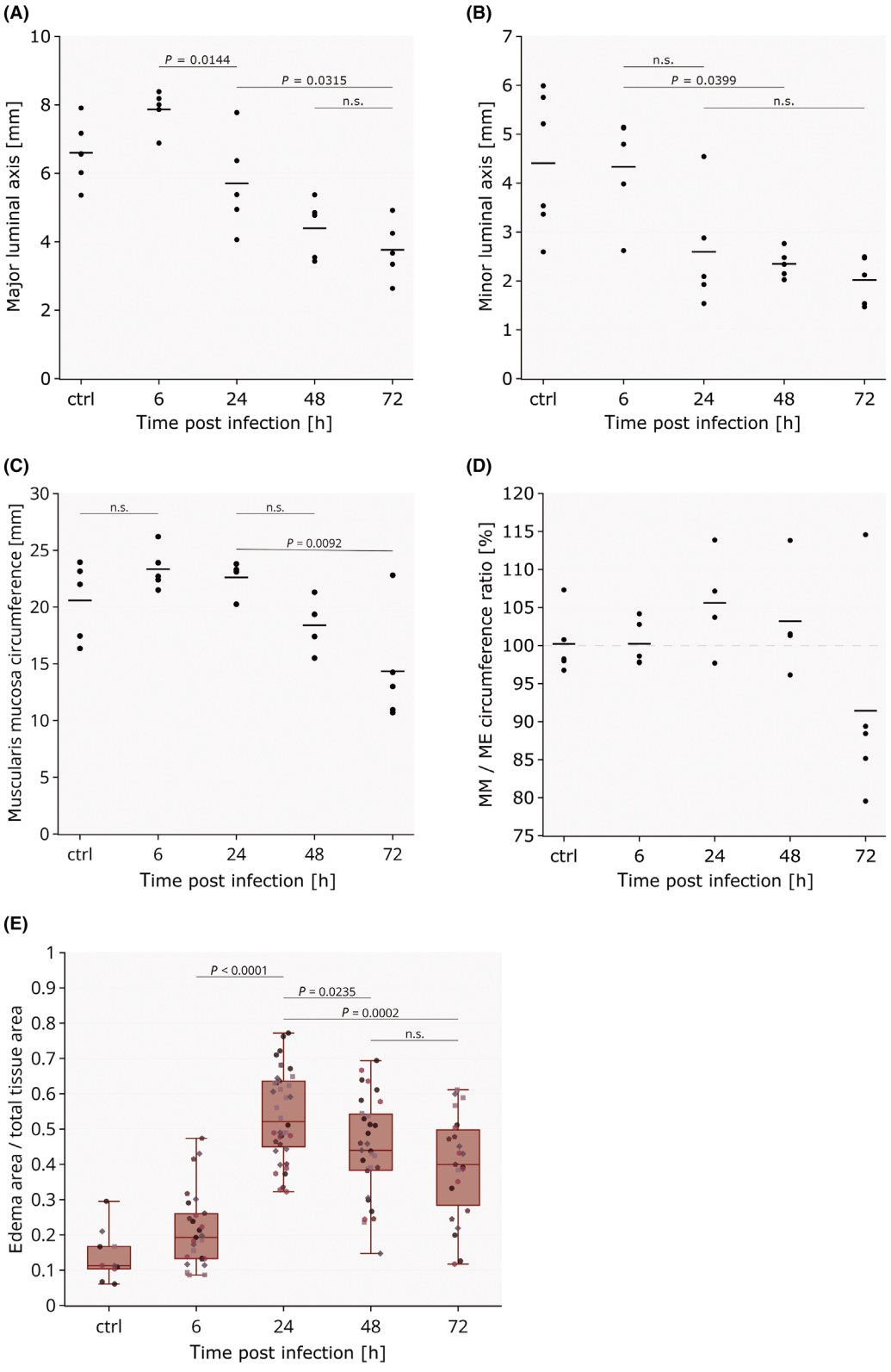

Fig. 2. Quantitative morphological analysis of *S.* Tm-infected cecum in C57BL/6 mice shows decrease of the cross-sectional luminal diameter with progressing infection time as well as submucosal edema formation from day 1 onwards. (A, B) Quantification of the major (A) and minor (B) luminal axis represents the strong volume decrease of the cecal lumen over the disease course. (C) The muscularis mucosa circumference is decreasing with progressing infection time supporting the reduction of cecum size. (D) Quantification of the ratio between muscularis mucosa (MM) length and muscularis externa (ME) length, unravels a strong decrease in the ratio between the two smooth muscle layers at 72 h postinfection reflecting the morphological change of the muscularis mucosa layer. (E) Quantification of the edema fraction of the total tissue cross-sectional area at four different timepoints and in control mice from H&E-stained cryosections, identifies largest edema fraction at 24 h postinfection. Datapoints represent individual tissue sections analyzed and boxplots extend from the first to the third quartile with median indicated as horizontal line. Different marker symbols identify the individual mice ($n = 5$) per timepoint. The whiskers represent the largest/lowest datapoint of the dataset that falls within 1.5× the interquartile range. (A–D) Datapoints represent averaged values for 4–5 individual mice per group, which were calculated from at least 3 H&E-stained cryosections per mouse. Horizontal lines indicate the mean value of the different groups. Statistical analysis: One-way ANOVA with Tukey's multiple comparison test, *P*-values indicated, n.s.: $P \geq 0.05$. H&E, hematoxylin & eosin; S. Tm, *Salmonella enterica* subspecies *enterica* serovar Typhimurium.

Intestinal edema contains stretched fibronectin fibers, while the adjacent smooth muscle layers show increasing fibronectin fiber relaxation as the infection progressed

Growing evidence supports an active role of extracellular matrix and its remodeling in the process of edema formation [45,46]. ECM remodeling not only affects stiffer scaffolding proteins such as collagens [47], but also elastic fibers, proteoglycans and glycoproteins such as fibronectin, which is known to interconnect parts of the ECM via a plethora of binding partners as well as for its mechanosensitive signaling abilities [23,26,48]. We used the FnBPA5 peptide to investigate the tensional state of fibronectin fibers in cryosections [37]. To control for unspecific binding of FnBPA5, a scrambled version of the peptide (scrFnBPA5) containing the same individual amino acids but ordered in a different sequence was applied. Fluorescently labeled scrFnBPA5 demonstrates the absence of unspecific, non-mechanosensitive binding of the peptide to fibronectin fibers as shown previously [37].

Twenty micrometer thick cryosections of cecum at different timepoints (6, 24, 48 and 72 h p.i.) were thus used to stain for total fibronectin using a polyclonal fibronectin antibody and the FnBPA5 peptide coupled to Cyanine5.5 (Fig. 4A). FnBPA5 signal in the muscularis externa significantly increased after 24 h and increased further over the next 2 days. In the late stage of the inflammation (72 h p.i.), small occasional clusters of FnBPA5 stains become visible in the mucosa, although this is not sufficient to significantly affect the overall mucosal average FnBPA5 signal (Fig. 4B). Surprisingly, there was no evidence for FnBPA5 binding in the edema regions at any timepoint of the disease (Fig. 4A,C). This was unexpected, as inflammation-associated proteases capable of cleaving fibronectin were anticipated to be present in high concentrations in the edema. Total fibronectin intensity values remained quite constant during the disease course in all tissue layers (Fig. 4D). Quantification of the intensity ratio of relaxed fibronectin to total fibronectin to control for variations in the fibronectin intensity levels, corroborates the low levels of FnBPA5 in edema during the disease progression (Fig. 4E). The specific absence of fibronectin fiber relaxation in edema contrasts with observations made in tumor models, where the fraction of structurally relaxed fibronectin fibers is increased with respect to healthy organs [36,38]. This suggests the potential role of stretched fibronectin fibers in counteracting edema swelling, which could help to maintain tissue integrity in intestinal edema. If this hypothesis is correct, we suspect that mechanisms are in place to protect fibronectin fibers against proteolytic cleavage at these sites. To investigate this further, we established a workflow to identify the edema-specific proteome.

Intestinal edema protein composition revealed by laser capture microdissection coupled to high-sensitivity mass spectrometry proteomics

Identifying the composition of intestinal edema is methodologically quite challenging as the contribution of edema to the overall tissue proteome is small. Therefore, laser capture microdissection was employed to extract edema areas from cecum sections of day 3 *S.* Tm-infected mice. Edema tissue areas were collected from serial 20 µm thick cryosections to match a total tissue volume of approximately 0.02 mm^3. This small amount of tissue required an optimized procedure during the sample lysis, protein precipitation and digestion (see materials and methods). The digested samples were loaded onto EvoTip Pure tips and were run on an Orbitrap Exploris mass spectrometer using data-independent acquisition (DIA) mode and a standardized acquisition method [49]. The raw files were analyzed using DIA-NN, a software developed to process

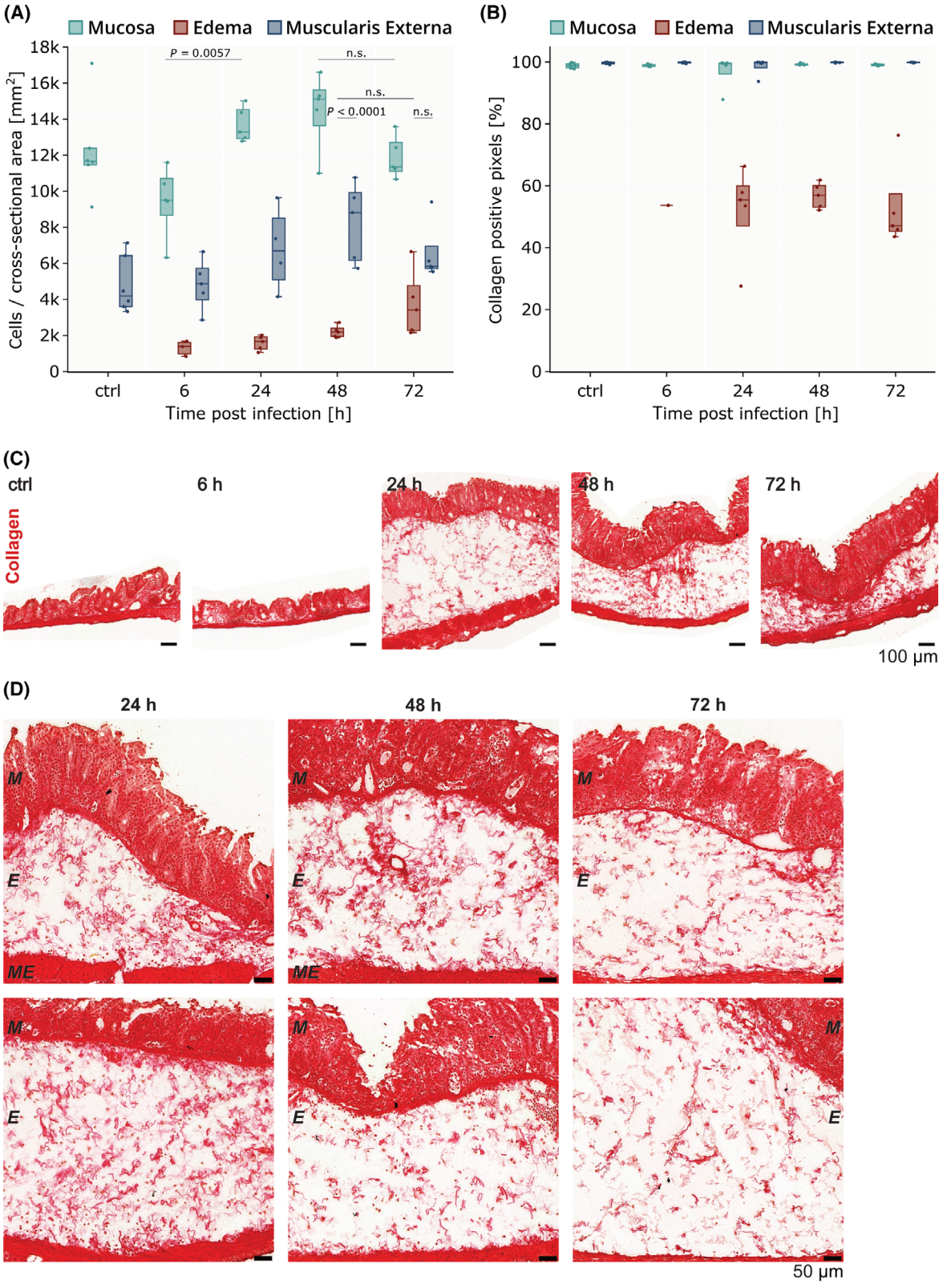

Fig. 3. Cell numbers and collagen content are strongly reduced in the submucosal edema areas compared to the rest of the *S.* Tm-infected cecum. (A) Quantification of cell numbers per area in the three different tissue areas (mucosa: green, edema: red, muscularis externa: blue) using H&E-stained cryosections, confirms the low cell density in edema relative to the other tissue layers. Statistical analysis: One-way ANOVA with Tukey's multiple comparison test, *P*-values indicated, n.s.: $P \geq 0.05$. (B) Sparse collagen content in edema areas was quantified by calculating the collagen positive pixel density in the three different tissue areas from picrosirius red-stained cryosections. Datapoints represent averaged values calculated from at least three H&E-stained sections per mouse from five individual mice per timepoint. Boxplots extend from first quartile to third quartile with median indicated as horizontal line. The whiskers represent the largest/lowest datapoint of the dataset that falls within 1.5× the interquartile range. (C) Representative picrosirius red-stained cecal sections during the disease timecourse (left to right: control mouse, 6, 24, 48 and 72 h postinfection), demonstrate the dispersed collagen signal in edema. Scale bar: 100 μm. (D) Additional higher magnification picrosirius red-stained cecal sections during the acute inflammation (24–72 h postinfection), representing the sparse and dispersed collagen network in the submucosal edema. Scale bar: 50 μm.

highly complex DIA data using deep neural networks [50]. A graphical schematic of the workflow is presented in Fig. 5A.

In total, 3798 unique proteins could be identified from which 1753 were found present in all 5 infected mice investigated. Gene Ontology (GO) analysis of these 1753 proteins using Metascape could identify 1534 matched proteins with the Metascape database [51]. Reassuringly, the analysis revealed the statistically enriched GO terms "Neutrophil degranulation", "cellular responses to stress" and "*Salmonella* infection" amongst other highly significantly enriched pathway terms. To give a general overview of the proteins that were found in the edema tissue, Fig. 5B represents a cluster map of the most significantly found GO terms. Interestingly, "supramolecular fiber organization" was the fifth most significantly enriched cluster, highlighting the importance of fiber reorganization in *S.* Tm--induced edemas (Fig. 5C).

To deepen our analysis, we then looked into the abundances of individual proteins and protein classes. Importantly, as an edema can only occur in diseased tissue, a relevant comparison to a "healthy control state" is not possible. The submucosal tissue layer in the cecum is barely visible in a healthy, non-infected mouse and thus cannot be analyzed separately from the other tissue layers. Therefore, relative abundances of edema proteins are presented and will be discussed in the scope of already existing knowledge about edema generation, with a major focus on involvement of ECM in this process. The most abundantly detected peptides mapped to the three fibrin(ogen) chains (alpha, beta, gamma) important for fibrin clot formation as well as mediating inflammatory responses, and to the cytoskeletal components actin, keratin type I and II, and myosin (Fig. 5D).

The importance of blood coagulation components, with fibrin(ogen) as a key player, is further strengthened by the GO enriched cluster "Hemostasis". To verify the finding that fibrin(ogen) was found in such high abundances in edema, we performed immunohistochemistry staining on cecal sections from healthy and day 3 *S.* Tm-infected mice. A clear increase in total fibrin(ogen) signal in the tissue could be seen in the severely inflamed tissue compared to healthy controls (Fig. 5F). The highest fibrin(ogen) intensities were observed in the edema regions, showing 2.5-fold and almost 5-fold higher mean fluorescence intensity between edema regions and the rest of the healthy and inflamed tissue, respectively (Fig. 5H). It is important to point out here that this observation cannot be solely explained by posthumous blood clotting, since inflamed and control tissues were handled identically, and we find a significant increase in edematous fibrin(ogen) content from the immunohistochemistry staining as well as the proteomics data between these two conditions. Comparing the abundance of all three fibrin(ogen) chains detected in the proteomics dataset, revealed a 47-fold increase comparing edematous fibrin(ogen) abundances with total healthy tissue (combining mucosal and muscularis externa proteomics data of healthy mice) (Fig. 5E). Co-staining with fibronectin revealed a fibrous fibrin-fibronectin matrix with visual similarity to those found in wound healing (Fig. 5G).

Identification of matrisome-specific proteins

The proteomics dataset was analyzed with a special focus on extracellular matrix proteins. One hundred and twenty-five from the 1753 proteins detected in all mice could be mapped to the matrisome database generated and curated by Naba *et al.* [52]. The matrisome can be separated into the core matrisome as well as matrisome-associated proteins. Figure 6A shows the distribution of matrisome proteins found in our edema tissues. In the core matrisome we found 63% of ECM glycoproteins, 16% of proteoglycans and 21% collagens, comprised of 12 different collagen family members. Strikingly, the majority of proteins in the matrisome-associated protein group were ECM regulators such as multiple members of the SERPIN family

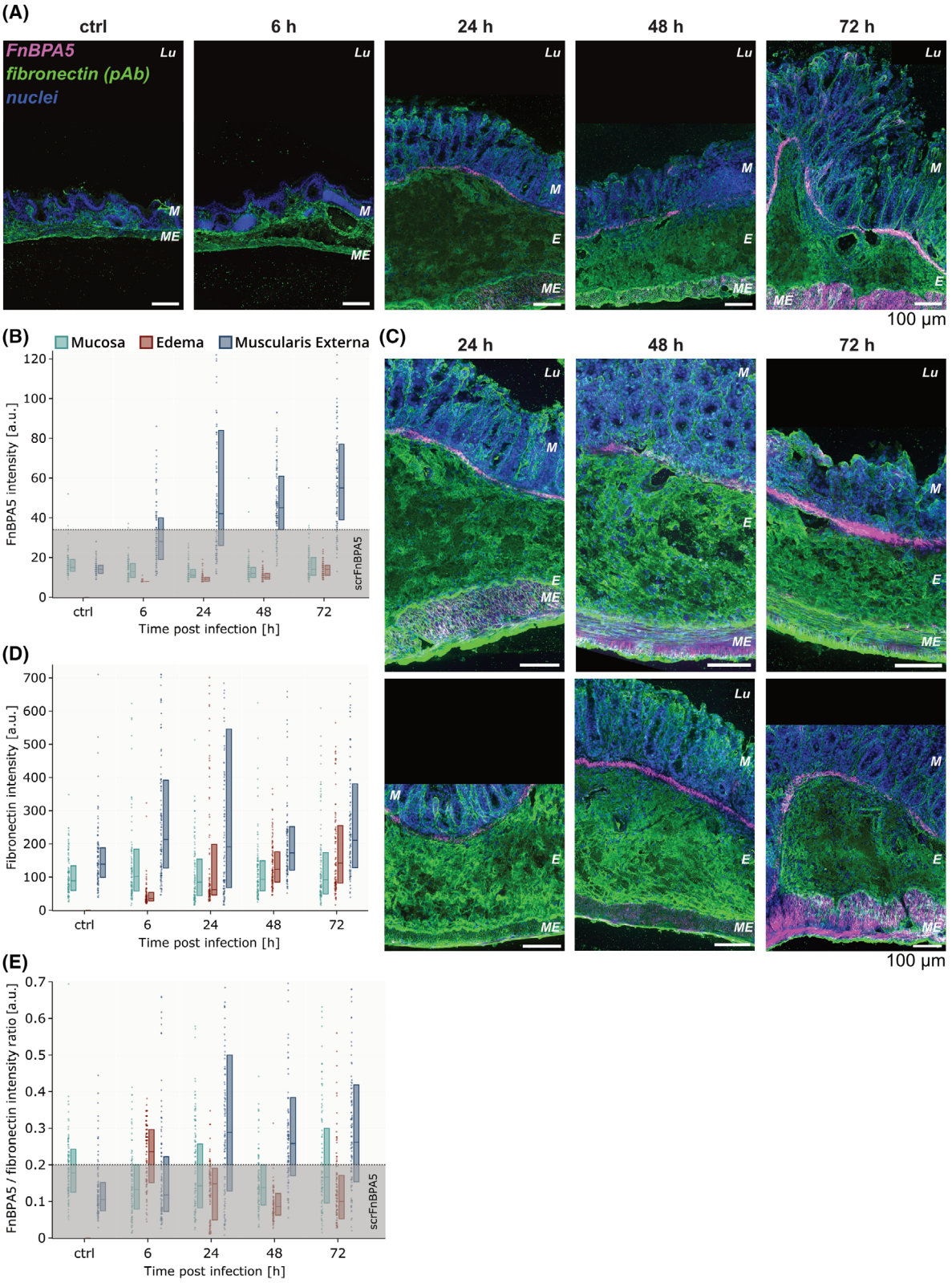

Fig. 4. Mechanobiological analysis of the *S.* Tm-infected cecum in C57BL/6 mice during the 3-day disease timecourse. (A) Representative images of immunohistochemistry staining of total fibronectin using a polyclonal anti-fibronectin antibody (green), relaxed fibronectin fibers using Cy5.5-FnBPA5 (magenta), as well as cell nuclei (blue) during the inflammation (left to right: control mouse, 6, 24, 48 and 72 h postinfection) Scale bar: 100 μm. (B) Pixel-by-pixel quantification of FnBPA5 intensity in the three tissue layers (mucosa: green, edema: red, muscularis externa: blue) at the same timepoints, respectively. Boxplots extend from first quartile to third quartile with median indicated. A subset of pixel intensity values ($n = 100$) as individual datapoints presented left to the boxplot to visualize the distribution. The gray box represents the averaged intensity of the scrFnBPA5 control staining (mean intensity value + 3 × standard deviation). (C) Additional representative images of immunohistochemistry-stained cecum (same staining as in A) during the acute inflammation (24–72 h postinfection). (D, E) Pixel-by-pixel quantification of fibronectin intensity and the FnBPA5/fibronectin intensity ratio in the three tissue layers at the same timepoints, respectively. Boxplots extend from first quartile to third quartile with median indicated. A subset of pixel intensity values ($n = 100$) as individual datapoints presented left to the boxplot to visualize the distribution. The gray box represents the averaged intensity of the ratio of the scrFnBPA5 control staining (mean intensity value + 3 × standard deviation) to the fibronectin intensity. *E*, edema; *Lu*, lumen; *M*, mucosa; *ME*, muscularis externa; pAb, polyclonal antibody; *S.* Tm, *Salmonella enterica* subspecies *enterica* serovar Typhimurium.

(59%). Serpins are a group of protease inhibitors that inhibit target enzymes by inducing a conformational change. They thus have major functions in hemostasis, since keeping the activities of serine proteases in check is essential to regulate blood coagulation [53], as well as in infection and inflammation [54]. ECM-affiliated proteins such as annexins, galectins and cathepsins as well as secreted factors such as the members of the protein S100 family make up 30% and 10% of the matrisome-associated protein class, respectively. Galectins are small carbohydrate-binding proteins with intra- and extracellular functions, where they modify interactions with and within the extracellular matrix, as well as with microbes [55]. Cathepsins are lysosomal proteases that get released into extracellular space upon tissue damage. The calcium-binding S100 proteins, when released from the cytoplasm upon tissue damage, serve as a danger signal, as they are crucial in the regulation of immune homeostasis, post-traumatic injury, and inflammation [56]. They can also enhance the adhesion and migration of leukocytes to the site of injury [57].

ECM-specific proteins in edema are involved in blood coagulation and in the negative regulation of peptidase activity

To investigate the functions of these matrisome annotated proteins, an ECM-specific GO enrichment analysis was performed. The top hits were related to extracellular matrix remodeling, regulation of blood coagulation, as well as negative regulation of peptidase activity (Fig. 6B). The most abundantly detected peptides mapped to 15 proteins including fibrin(ogen), decorin, fibronectin and various collagen chains (I, VI, XIV). Interestingly, the edema-specific matrisome network assembles around fibronectin as the core protein, confirming its central role in edema formation and matrix remodeling (Fig. 6C). The exact influence of the detected matrisome proteins on inflammation is difficult to infer from our dataset, since collagens, decorin and fibronectin all have distinct pro- and anti-inflammatory properties and any intervention will have a narrow window between influencing disease kinetics and causing disastrous loss of tissue integrity, i.e. such interventions go beyond the scope of this study [58]. Nevertheless, the high number of secreted ECM proteins suggests an effort to stabilize, rebuild, and repair the damaged ECM, which is in line with other wound healing and tissue remodeling situations such as skin wound sites [59,60]. The regulation of blood coagulation seems to be very important and in fact it would be highly interesting in the future to investigate the role of the coagulation pathway in *S.* Tm infection biology in more detail. Simultaneously, this observation is very hard to study in *in vivo* models due to the association of anti-coagulation drugs with gastrointestinal bleeding, which was exemplified by strong exacerbation of less excessive tissue inflammation models by anticoagulant administration in mice [61]. Our findings of high levels of fibrin(ogen) together with fibrillar, stretched fibronectin suggest that there are active tissue stabilization and early wound healing processes ongoing in the edema during acute non-typhoidal *Salmonellosis* in the mouse cecum.

Protease and protease inhibitor network in intestinal edema

To better understand why mostly stretched fibronectin fibers were detected in edema, we looked further into tissue remodeling processes with a focus on specific proteases and protease inhibitors present in our dataset. For this, we extended the analysis again to the whole dataset (proteins found in edema of all 5 mice, not

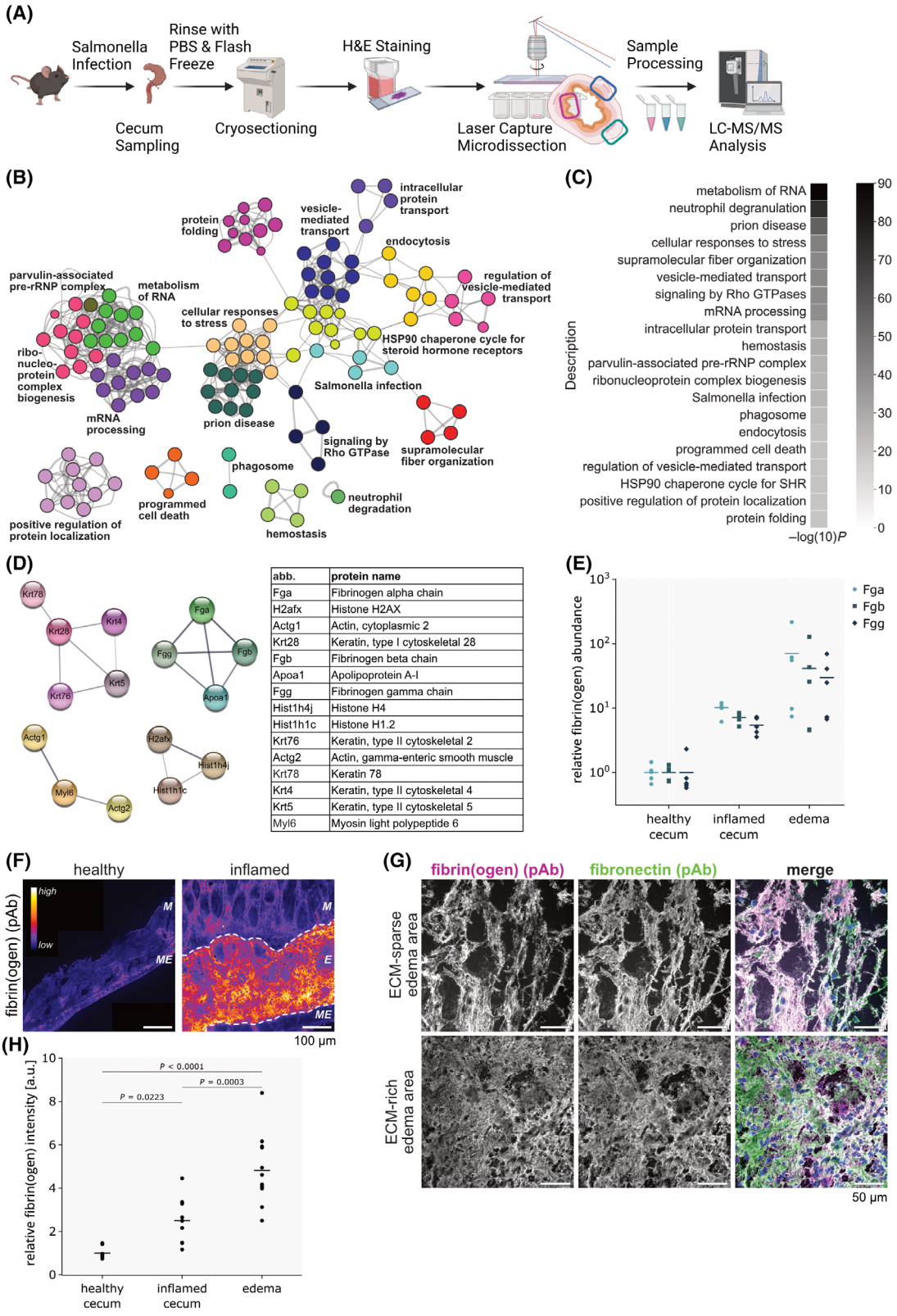

abb.	protein name
Fga	Fibrinogen alpha chain
H2afx	Histone H2AX
Actg1	Actin, cytoplasmic 2
Krt28	Keratin, type I cytoskeletal 28
Fgb	Fibrinogen beta chain
Apoa1	Apolipoprotein A-I
Fgg	Fibrinogen gamma chain
Hist1h4j	Histone H4
Hist1h1c	Histone H1.2
Krt76	Keratin, type II cytoskeletal 2
Actg2	Actin, gamma-enteric smooth muscle
Krt78	Keratin 78
Krt4	Keratin, type II cytoskeletal 4
Krt5	Keratin, type II cytoskeletal 5
Myl6	Myosin light polypeptide 6

Fig. 5. Investigation of the intestinal edema-specific proteomic signature in *S.* Tm-infected C57BL/6 mice at day 3. (A) Schematic of workflow for edema-specific proteomics analysis using laser capture microdissection. Individual tissue areas were extracted from H&E-stained cryosections. Illustration generated using BioRender.com. (B) Overview of all identified Gene Ontology clusters color-coded by similarity. Labels are based on the most representative GO term in the cluster. (C) Quantification of GO enriched terms of all proteins detected in cecal edema. (D) Top 15 proteins matched to most abundantly detected peptides represented as network (connecting line thickness scaling with the combined STRING score) as well as table (sorted by detection abundance). (E) Quantification of fibrin(ogen) abundance from the edema-specific proteomics dataset and comparison with total healthy and inflamed tissue (without edema tissue area) abundance. Fibrin(ogen) alpha (Fga), beta (Fgb) and gamma (Fgg) chain quantified separately (circle, square, diamond markers, respectively). Datapoints represent individual mice (healthy: $n = 5$; inflamed $n = 5$) with the mean indicated as horizontal bar. (F) Representative image of immunohistochemistry staining of fibrin(ogen) in healthy and inflamed (72 h postinfection) cecum sections using a polyclonal anti-fibrin(ogen) antibody, shows strong accumulation in the edema. Scale bar: 100 μm. (G) Representative images of co-staining for fibrinogen (magenta) and fibronectin (green) in a sparse (upper panel) and a less-sparse (lower panel) region of cecal edema, visualize the closely associated network of the two proteins. Scale bar: 50 μm. (H) Quantification of the fibrin(ogen) signal intensity in overall healthy cecum tissue (muscularis mucosa and muscularis externa) and the relative to this normalized signal intensities in overall inflamed (muscularis mucosa and muscularis externa) as well as in edema-specific tissue areas, shows significant increase of fibrin(ogen) intensity in edema tissue. Horizontal lines indicate the mean value of the different groups. Datapoints represent analyzed images from healthy and inflamed (72 h postinfection) mice (10 images of healthy mice ($n = 3$) and 12 images of inflamed mice ($n = 3$) analyzed for the different categories). Statistical analysis: One-way ANOVA with Tukey's multiple comparison test, *P*-values indicated, n.s.: $P \geq 0.05$. *E*, edema; ECM, extracellular matrix; H&E, hematoxylin & eosin; LC–MS/MS, liquid chromatography with tandem mass spectrometry; *M*, mucosa; *ME*, muscularis externa; pAb, polyclonal antibody; PBS, phosphate-buffered saline; *S.* Tm, *Salmonella enterica* subspecies *enterica* serovar Typhimurium.

limited to the matrisome database mapped proteins only). Using the PANTHER database, we allocated protein classes to the protein hits we found [62,63]. Our dataset contains 67 proteins matched to the PANTHER protein class "proteases" as well as 28 proteins allocated to the class "protease inhibitors". The protease class can be further broken down into 13 cysteine proteases, 13 metalloproteases, 10 serine proteases, 1 aspartic protease as well as 30 unspecified proteases containing mostly proteasome components. The relative abundances with which these proteins were found in the edema of all 5 mice are presented in a protein–protein network format in Fig. 7. Manual detailed curation of the dataset using the MEROPS database [64], revealed the presence of several known fibronectin-targeting proteases. Matrix metallopeptidases-3, -8, and -10 were detected in the edema tissues as well as the cysteine protease legumain (Lgmn: Uniprot accession: O89017), which was shown to cleave fibronectin [65]. Interestingly, the reported inhibitor of Lgmn, Cystatin-C (Cst3: Uniprot accession: P21460) was also found with similar abundance. Additionally, we detected the protease inhibitor calpastatin (Uniprot accession: P51125) together with its targets calpains in the protease network. Calpastatin is known for inhibiting calpain 1 (Uniprot accession: O35350) and calpain 2 (Uniprot accession: O08529), which in turn were shown to have in addition to their intracellular activity, also extracellular fibronectin fragmentation activity [66,67]. Overall, this shows multiple protease inhibition possibilities in the *S.* Tm-induced edema to protect fibronectin fibers from getting cleaved.

Discussion

To address the impact of ECM in tissue stabilization and repair during gastrointestinal inflammation, we characterized cecal tissue alterations during inflammation from a biochemical and mechanobiological perspective. We identified the proteomic signature of intestinal edema in the late stage of the *S.* Tm infection in mice and revealed the presence of tensed fibronectin fibers and of a large protease and protease inhibitor network mostly tracing back to the blood coagulation pathway in intestinal edema.

In general, intestinal tissue is subjected to a plethora of mechanical forces under normal as well as pathological conditions. These physical forces act at all length scales, from the macroscopic to the molecular level, including muscular contractions [68], shear stress, cell–cell interactions, and lymphatic flow [69–71]. During tissue inflammation these forces are altered and can induce changes in cellular mechanotransduction processes [72]. Consistent with the previously reported shrinkage of the cecum during *S.* Tm infection [10], we observe a significant reduction of luminal area as well as a change in circumference of the two prominent smooth muscle cell layers, muscularis mucosa and muscularis externa. In the healthy cecum, the two muscle layers show a circular structure and are in close proximity to each other. Upon the onset of the inflammation, the muscularis mucosa along with the mucosal layer switch from this circular to a more buckled morphology. The luminal volume loss seems to be steered by both the contractions of the smooth muscle layers

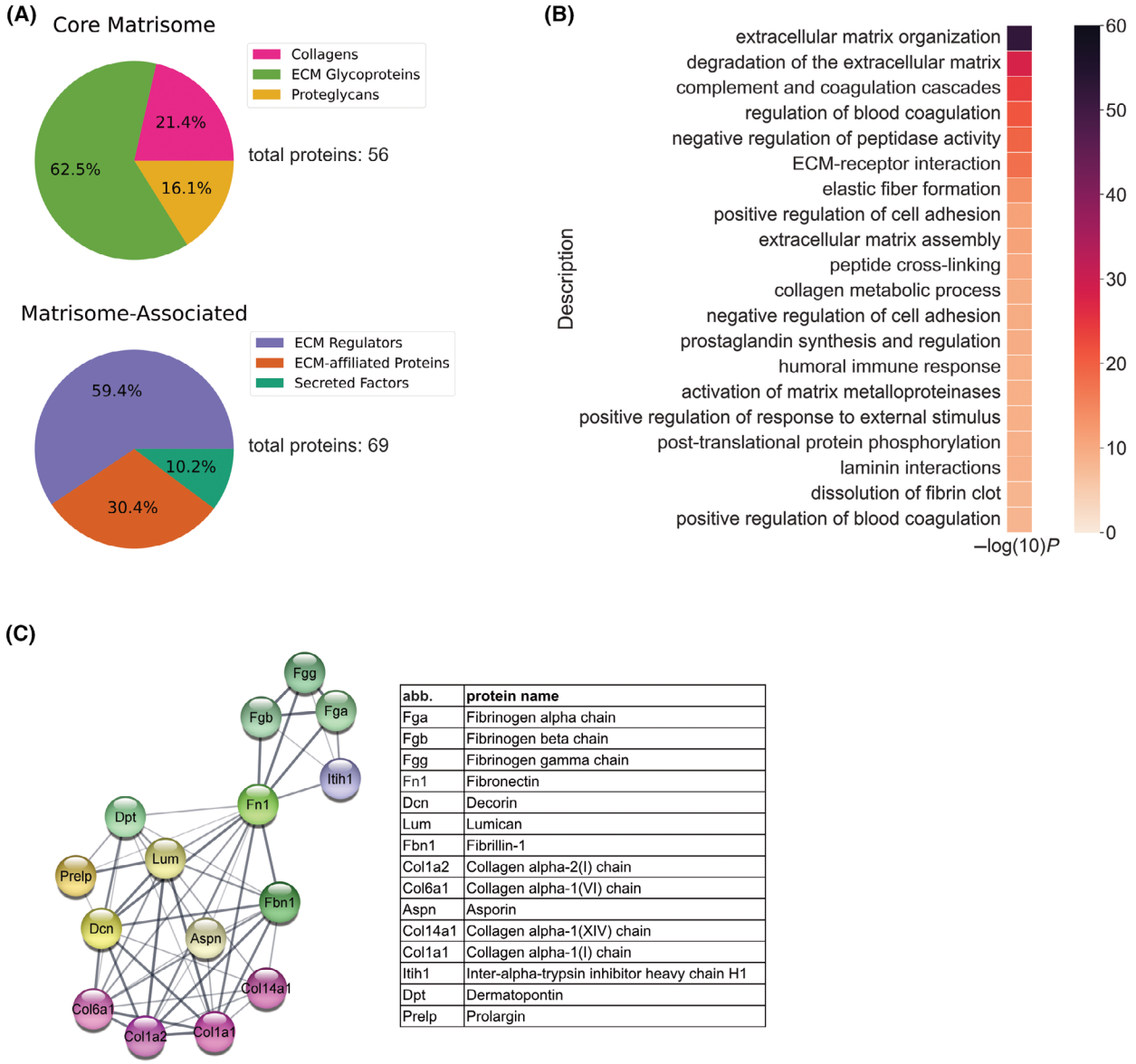

abb.	protein name
Fga	Fibrinogen alpha chain
Fgb	Fibrinogen beta chain
Fgg	Fibrinogen gamma chain
Fn1	Fibronectin
Dcn	Decorin
Lum	Lumican
Fbn1	Fibrillin-1
Col1a2	Collagen alpha-2(I) chain
Col6a1	Collagen alpha-1(VI) chain
Aspn	Asporin
Col14a1	Collagen alpha-1(XIV) chain
Col1a1	Collagen alpha-1(I) chain
Itih1	Inter-alpha-trypsin inhibitor heavy chain H1
Dpt	Dermatopontin
Prelp	Prolargin

Fig. 6. Matrisome-specific protein network detected in *S.* Tm inflammation induced intestinal edema at day 3 in C57BL/6 mice. (A) Affiliation of detected edema proteins to the six different matrisome categories. Fifty-six proteins detected are affiliated to the core matrisome category (ECM glycoproteins: 62.5%, collagens: 21.4%, and proteoglycans: 16.1%). In the matrisome-associated category, 69 proteins were detected (ECM regulators: 59.4%, ECM-affiliated proteins: 30.4%, and secreted factors: 10.2%). (B) Quantification of Gene Ontology enriched terms of matrisome-specific proteins detected in cecal edema. (C) Top 15 matrisome-specific proteins matched to most abundantly detected peptides represented as STRING network as well as table (sorted by detection abundance), highlighting the important role of fibronectin in this network (connecting line thickness scaling with the combined STRING score). ECM, extracellular matrix; *S.* Tm, *Salmonella enterica* subspecies *enterica* serovar Typhimurium.

and the increasing tissue volume, driven by increased mucosal thickness and edema built up in the submucosa. Reducing the potential volume that luminal *Salmonella* can colonize is an obvious benefit to the host. However, the forces created by massive fluid influx thereby are challenging tissue integrity as the inflammation progresses. The buckling of the inner muscle layer during the first 2 days of bacterial infection maintains anchor points between the inner and outer muscle layers despite edema formation, however, this anchorage is mostly lost on day 3. The circular structure of the inner muscle layer in the presence of

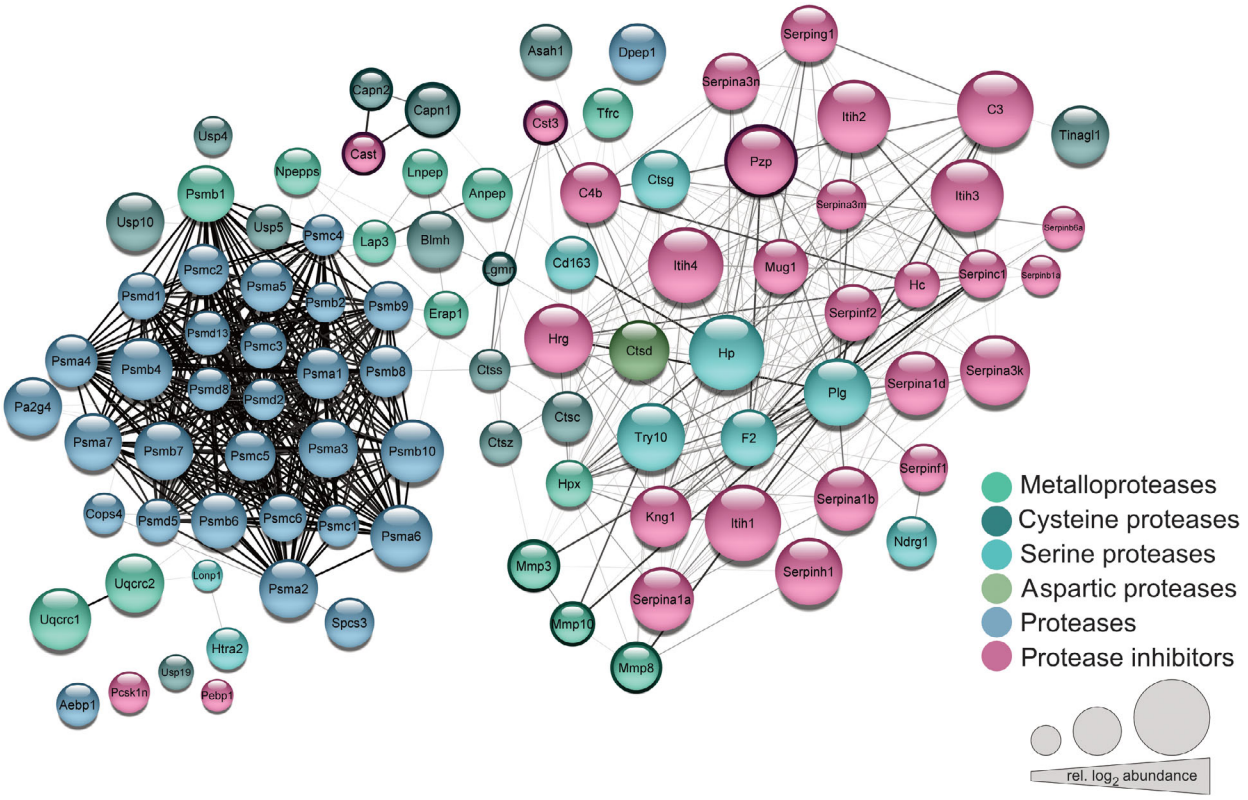

Fig. 7. Protease – protease inhibitor network in intestinal edema at day 3 in C57BL/6 mice. Intestinal edema-specific protease–protease inhibitor network revealed 67 proteases and 28 protease inhibitors. Multiple proteases with fibronectin cleavage capability were detected together with their protease inhibitors (highlighted with dark border). Legumain (Lgmn) with its inhibitor cystatin-C (Cst3) as well as the network of calpains (Capn1 + 2) with their inhibitor calpastatin (Cast) are highlighted. General MMPs (-3, -8, 10) important for matrix remodeling and affiliated serpin inhibitors are shown as well as the broad-spectrum protease inhibitor pregnancy zone protein (Pzp). The circle color represents the protein class (protease inhibitors, proteases, metalloproteases, cysteine proteases, serine proteases, and aspartic proteases) and the circle size the relative $\log_2$ abundance with which this protein was detected in the dataset. Of note, while absolute quantification was not possible, typically higher peptide counts were observed for protease inhibitors compared to cysteine-, serine- and metalloproteases. The gray lines represent protein associations predicted using the STRING database (connecting line thickness scaling with the combined STRING score).

edema might thus indicate one step towards full tissue disintegration of the inflamed cecum in *S.* Tm-infected C57BL/6 mice, as this infection is typically lethal on day 4/5 in this model [73].

To ask whether molecular mechanisms might have evolved to reduce the risk of tissue rupture in severe inflammation, we further characterized the molecular composition and ECM properties of *S.* Tm-induced intestinal edema. It contained a fibrous network of matrix components, especially a comparatively sparse, disorganized, and fragmented collagen fiber network, and a limited number of cells. The well-validated fibronectin tension sensor FnBPA5 [33,35–38] only binds to low tension but not to tensed fibronectin fibers, as fiber stretching and partial domain unfolding destroys its multivalent binding motif [33,35]. Co-staining utilizing a polyclonal fibronectin antibody and the fibronectin binding peptide FnBPA5 revealed that fibronectin fiber tension in bacterially infected cecum tissue is dependent on the tissue layer. While fibronectin fiber relaxation is triggered after 1 day of infection already in the muscle layers, the tensed fibronectin fibers in the edema are present during the whole course of inflammation. Although a complete exclusion of potential hindrance from unknown binding partners competing with FnBPA5 for binding to the N-terminal domain of fibronectin in the edema cannot be completely excluded, the high FnBPA5 peptide affinity, the presence of fibronectin fibers confirmed by antibody binding, and the internal control of positive FnBPA5 stainings in the muscularis layers, collectively support the hypothesis that fibronectin fibers are under tension and serve a load-bearing function in the intestinal edema. Tensing

fibronectin fibers might help to delay tissue disintegration as fibronectin fibers are known for their capability of force-induced extension and contraction, once the tensile forces are released. Fibronectin's multifold extensibility is associated with structural unfolding of various of its domains [30,74,75], which is reversible [26,44,75,76]. Fibronectin fibers can expand to more than 6-fold *in vitro* and recover first the original contour length and subsequently their mechanical stability, which requires domain refolding within minutes after release [44]. Upon stretching, they can thus store elastic energy. On release of applied forces or acting hydrostatic pressure, the refolding of the fibronectin domains will shorten the fibers and thereby have the capacity to pull its anchor points into closer proximity. This could help to pull the muscularis mucosa and muscularis externa into closer proximity and thereby support the reconstruction of tissue integrity. Due to the low amount of collagen and its disrupted fiber network observed, as well as the low number of cells in cecal edema, we hypothesize that fibronectin fibers may actually be the main force-bearing structural component in intestinal edema, perhaps in part counterbalancing the disruptive forces imposed by the build-up of hydrostatic pressure between the inner and outer muscle layer. The use of a collagen hybridizing peptide (CHP), which binds to denatured collagen helices indeed suggests the presence of mechanically or biochemically damaged collagen fibers. It is thus conceivable that fibronectin fibers within a network of fibrin might take over as force-bearing elements [29] and serve as "bungee" cords keeping the inner and outer muscle layers connected even in locations where massive fluid influx leads to their spatial separation.

Interestingly, the finding of stretched fibronectin fibers in inflamed intestinal edema stands in stark contrast to other pathological tissue transformations, where the tensional state of fibronectin fibers has been mapped by the same FnBPA5 tension probe. In tumor tissues, a significant fraction of fibronectin fibers is found in a relaxed conformation in contrast to healthy organ tissues where the fibronectin fibers were dominantly tensed. The areas of relaxed fibronectin fibers in cancer tissues spatially correlated with straightened fibrillar collagen bundles as probed by second harmonic generation imaging [36–38]. Proteolytic degradation of fibronectin fibers, or the increased fibrillar collagen density in tumor tissues could enable fibronectin fiber relaxation, as collagen fibers can take over at least in part the role as force-bearing structural elements [29,37]. In intestinal edema, however, the collagen fibers look fragmented suggesting that an intact collagen fiber network is mostly missing. Fibronectin might thus be left with the task to carry tissue mechanical stresses. Additionally, studies on lymph nodes, identified relaxed fibronectin fibers in severely inflamed, virus-infected lymph nodes, while the fibronectin fibers are stretched in adjuvant treated, swollen as well as naïve lymph nodes [36]. This is highly interesting since the fibronectin fiber tension seen in the intestinal edema of bacterially infected mice shows similarities with the adjuvant swollen but not with the virus-infected lymph node.

At the molecular level, it is quite surprising that fibronectin fibers are not cleaved in the inflamed tissue, as the infiltrating tissue fluid is typically rich in proteases. Via proteomics on laser capture dissected edema tissues, we identified multiple proteases, which are capable of cleaving fibronectin (MMP-3, MMP-8, Lgmn, Capn). Based on our tissue stains, we hypothesize that there are distinct protease inhibitor mechanisms in place protecting stretched fibronectin fibers from degradation, specifically in the intestinal edema. This hypothesis was indeed supported by the detection of multiple members of the SERPIN superfamily, pregnancy zone protein, cystatin-C (Lgmn inhibitor), and calpastatin (Capn inhibitor) (Fig. 7). Although absolute quantification in untargeted proteomics is not possible, we typically observed higher peptide counts for protease inhibitors than for cysteine-, serine-, and metalloproteases, consistent with this hypothesis.

Taken together, we would like to propose that fibronectin fibers in the submucosa of the intestine might serve so far unrecognized mechanical functions, i.e. by helping to maintain tissue integrity across regions of edema during intestinal inflammation through mechanical stretching and ultimately retraction of fiber tension when the inflammation subsides. As the submucosa swells, the fibronectin fibers, intermingled with fibrin networks, interconnect the two muscle layers. They get extended as the fluid volume separating the two builds up, thereby keeping the muscle layers connected. Fibronectin's ability to retract to its original length lets us speculate that these fibers might serve to store elastic energy to help contract the fluid-filled gap between the muscularis mucosa and muscularis externa in case of edema regression. Beyond the visualization of stretched fibronectin fibers, directly testing their mechanical function in edema is challenging. Microinjections of fibronectin-targeting proteases directly into edema in living mice at an early state of the infection (24 h p.i.) could provide insights but raise ethical concerns due to the required surgery on severely diseased mice and the potentially lethal consequences for the animals caused by the induced cleavage of fibronectin fibers. Due to the lethality of full fibronectin knockout in mouse embryos, studying edema swelling processes in the absence of fibronectin is impossible. Hence, *in vitro* 3D model systems such as organoids or tubular mini-guts [77] would offer more viable alternatives. However, these

models are currently very limited in replicating the complex multilayered tissue architecture and co-presence of immune cells necessary to elucidate fibronectin's role in edematous tissue integrity [78]. Future advancements in these culturing techniques to include realistic gut architecture and multiple cell types and signals might allow us to address the challenges and will help disentangle the role of fibronectin fibers in intestinal edema.

Extracellular matrix remodeling is an active process during intestinal inflammation, with apparent differences between the different layers of the intestine. Laser capture microdissection together with state-of-the-art LC–MS/MS-based proteomics on low amounts of biomass overcomes the limitations of bulk proteomics to delineate these processes. We could therefore identify candidate proteins involved in the regulation of intestinal remodeling during *Salmonella* infection. By combining these data with a novel fibronectin fiber tension sensor and (immuno)histochemistry microscopy, we observed an abundance of extended fibronectin fibers and fibrin network in intestinal edema, while collagen fibers were disrupted. The high extensibility of fibronectin fibers might thus delay rupture of the intestinal wall as swelling continues and might be vital to avoid further tissue integrity loss. Our data suggest that a provisional matrix composed of fibronectin/fibrin-based fibers takes over the load-bearing functions in edema. We have also identified high levels of both proteases and protease inhibitors in edema fluid, opening the door to the generation of protein/gene-based reporters to study edema formation in animal models, and potential pharmacological targeting of edematous intestinal inflammation. Understanding these mechanical processes, and knowledge of key proteases and protease inhibitors involved, may also provide valuable functional diagnostic markers of intestinal disease progression in the future.

Materials and methods

Ethics statement

All animal experiments were approved by the legal authorities (license ZH120/19; Kantonales Veterinäramt Zürich, Switzerland) and performed according to the legal and ethical requirements. Animals were scored daily for any expected or unexpected adverse events. Humane endpoints were defined in the license. Special focus was put on the 3R principles (Replacement, Reduction and Refinement) for humane animal handling.

Mice

All experiments were performed with male and female specific-pathogen-free C57BL/6J mice (10–11 weeks old) from an inbred colony at the ETH Phenomics center, and were housed in groups of 2–5 animals in individually ventilated cages in the ETH Phenomics center (EPIC, RCHCI), ETH Zürich. Water and food were given *ad libitum* during all times. Before the experiments, mice were trained to obtain a fruit-peanut mix (3 : 2 : 3 of 20% maltose solution, peanut oil (sterilized), and fruit puree (fruit puree containing apples (56%), bananas (30% and raspberry (14%), pasteurized))) from the micropipette once per day on two consecutive days. The mice were pretreated 1 day before the *S.* Tm infection with 25 mg of streptomycin (#15070063; Thermo Fisher Scientific, Waltham, MA, USA) in 75 µL sterile fruit-peanut solution via voluntary feeding. Twenty-four hours later the animals were infected with 5×10^7 CFU of *S.* Tm (75 µL suspension of sterile fruit-peanut solution) or treated with sterile fruit-peanut solution (control) by voluntary feeding. The *Salmonella* culture was prepared as overnight culture from wild-type *S. enterica* serovar Typhimurium clone SB300, a derivative of strain SL1344 [10], grown for 12 h in Lysogeny Broth (LB) medium containing 50 $\mu g \cdot mL^{-1}$ streptomycin at 37 °C. Then the bacterial culture was diluted 1 : 20 in fresh LB medium without antibiotics and the subculture was grown for 3 h at 37 °C. Before preparing the fruit-peanut suspension, the bacteria were washed twice in cold PBS. At the indicated times p.i. the mice were sacrificed by CO_2 asphyxiation followed by blood withdrawal from the heart and tissue samples were dissected for further processing. The mock infected control group was sacrificed together with the 72 h p.i. group. To avoid cage effects, the animals for the individual groups were combined from several cages. During the infection, the animals were scored daily.

Quantification of fecal Lipocalin2

Fecal pellets collected at the indicated timepoints were homogenized in PBS by bead-beating at 25 Hz for 2 min. Large particles were sedimented by centrifugation at 300 ***g*** for 1 min. The supernatant was analyzed using the mouse Lipocalin-2 enzyme-linked immunosorbent assay (ELISA) Duoset (DY1857-05; R&D Systems, Minneapolis, MN, USA) according to the manufacturer's instruction in serial dilutions.

Histological procedure

Whole ceca were dissected from the mice and thoroughly rinsed with PBS to remove the content and partially the mucus layer. Three to four washes with PBS using a rat gavage needle attached to a 20 mL syringe were required to achieve successful washing. In a second step, the ceca were filled with cryo embedding medium OCT (#4583; Tissue-Tek® O.C.T. Compound, Sakura Finetek Europe, the Netherlands) using a rat gavage needle coupled to a 2 mL OCT filled syringe to reach original organ expansion. Depending on the infection state, the volume to fill the

cecum varied. Then, ceca were embedded in OCT, snap-frozen in liquid nitrogen and stored at −80 °C until further processing. Cryosections for hematoxylin and eosin (H&E) stains and picrosirius red stains were cut at 10 µm thickness. Cryosections for immunohistochemical stains were cut 20 µm thickness (Thermo Scientific Cryostat Microm HM 525). Sections were mounted on glass slides, dried shortly at room temperature, and moved to −20 °C for further drying and short-term storage. For H&E stains and picrosirius red stains, sections were washed with PBS once before fixed with 4% Formaldehyde solution (#P087.3, ROTI®Histofix; Carl Roth, Karlsruhe, Germany) for 10 min and washed again 2× with PBS and 1× with distilled water. The H&E staining procedure was automated using a histology H&E stainer (COT 20; Medite AG, Burgdorf, Germany) and samples were embedded using Pertex mounting medium (#41-4014-00; Biosystems, Muttenz, Switzerland). For picrosirius red stains, sections were stained with Weigert's hematoxylin (8 min), washed with tap water, stained with Sirius Red Staining solution (1 h) and washed twice with 0.2% acetic acid in ethanol (30 s each). Then sections were dehydrated using 80%, 95% and 100% ethanol solutions (5 min each) and subsequently washed twice in xylol (5 min each) and embed using Eukitt (#03989; Merck, Darmstadt, Germany).

Immunohistochemical procedure

Co-stainings for relaxed (Cy5.5-FnBPA5) and total fibronectin (anti-fibronectin antibody) fibers as well as for fibrin(ogen) were performed as follows: Tissue sections on glass slides were encircled with a hydrophobic pen (Vector) to decrease staining solution usage. The tissues were then washed once with PBS and blocked with 4% BSA in PBS for 30 min. Cy5.5-FnBPA5 solution was diluted in PBS, added to the sections at a concentration of 5 $\mu g \cdot mL^{-1}$ and incubated for 1 h. For all these steps, 100 µL of solution was used per cryosection. The sections were then washed by immersing the whole glass slide into a beaker with PBS (3× 5 min each). In the next step, the tissue sections (20 µm thick) were fixed with 4% formaldehyde solution (#P087.3, ROTI®Histofix; Carl Roth) for 10 min and subsequently washed with PBS 3× for 5 min each. Then sections were blocked for 45 min using a blocking buffer containing 5% goat or donkey serum (depending on the host species of the secondary antibody) (#G9023 and #D9663; Merck) and 0.3 M glycine (#56-40-6; Merck) in PBS. Fibronectin was stained using a polyclonal anti-fibronectin antibody (ab23750; Abcam, Cambridge, UK) at a dilution of 1 : 100 and fibrin(ogen) using the polyclonal anti-fibrin(ogen) antibody (#4440-8004; BioRad, Hercules, CA, USA) at a dilution of 1 : 200 incubating over night at 4 °C in a humidified chamber. After three washes with PBS (5 min each), the secondary antibody goat anti-rabbit IgG Alexa 488 (A11043; Thermo Fisher Scientific) 1 : 200 (for fibronectin) or donkey anti-sheep IgG Alexa 488 (A-11015; Thermo Fisher Scientific) at 1 : 200 and donkey anti-rabbit IgG Alexa 647 (A10040; Thermo Fisher Scientific) at 1 : 200 (for Fibrinogen + Fibronectin) was applied for 1 h at room temperature. After a quick wash with PBS, co-stain with 4′,6-diamidino-2-phenylindole (DAPI) (D9564; Sigma Aldrich, St. Louis, MO, USA) was performed (10 $\mu g \cdot mL^{-1}$) for 10 min. Last, the sections were washed 3× for 5 min in PBS, dried and mounted using ProLong Gold antifade mounting medium (#P36930; Thermo Fisher Scientific). Mounted and stained sections were allowed to dry at room temperature and stored at 4 °C before image acquisition.

Collagen hybridizing peptide staining procedure

The collagen hybridizing peptide (CHP) staining procedure was performed following the protocol from the company 3Helix (Salt Lake City, UT, USA) [79]. In short, the Cy3-conjugated CHP was reconstituted in 1 mL of 1× PBS and vortexed well to prepare a stock solution (100 µM). For staining of the histology slides, the OCT medium was washed off with PBS, then the tissues were blocked with blocking buffer containing 10% goat serum in PBS and 0.3 M glycine. The Cy3-CHP was diluted to 5 µM (optimized concentration determined in a separate experiment for the intestinal tissue sections) and was heated 5 min at 80 °C. After immersing the CHP-containing tube into an ice-water bath for 15–90 s to avoid thermal damage to the tissue samples, 100 µL of the solution were added immediately to each tissue section. Here, avoiding dead times of more than 3 min has to be avoided to ensure that the CHP peptides do not start to reform into triple helices themselves. The samples were incubated at 4 °C overnight and were subsequently washed 3× for 5 min with PBS at room temperature. Unheated CHP was used as a negative control for CHP binding. The nuclei were counterstained with 2.5 $\mu g \cdot mL^{-1}$ DAPI in PBS for 20 min and the tissues were mounted with ProLong Gold Antifade mounting medium. After drying they were stored at 4 °C.

Microscopy

All histological stains were imaged using the automated Slide Scanner Pannoramic 250 (3D Histech, Budapest, Hungary). All immunohistochemistry stains were imaged using the Nikon Eclipse Ti2 microscope, equipped with the Yokogawa Confocal Scanner Unit CSU-W1-T2 and operated with the NIS-ELEMENTS software (Nikon Corporation, Tokyo, Japan). Images were acquired using a 60× 1.2 CFI Plan Apo VC Water Objective (Nikon Corporation). Z-stack multi-tile images at three different locations on the individual cecum section were acquired using a large image scan pipeline and stitched with the NIS-ELEMENTS software.

Quantification of tissue areas

Intestinal tissue layers were identified and segmented using a machine learning-based algorithm in QUPATH [80]. The algorithm was trained specifically to detect the three tissue layers muscularis externa, submucosal edema and mucosa. In order to improve the reliability of the quantifications, the analysis was performed on sections from two different parts in the cecum. The first one starting at the dead end of the cecum after trimming through the Peyer's patch cluster. The second set of sections was collected from the middle part of the organ with additional care for the cutting orientation of the organ. In short, three differently oriented sections per mouse were cut (turning the orientation 90° for every section). Cecal circumference, major luminal axis, as well as the ratio between the circumference of the muscularis mucosa and the whole tissue were determined by manual annotations in the CASEVIEWER software (CASE VIEWER 2.4; 3D Histech) designed to support examination of images acquired with the automated Slide Scanner.

Quantification of cell numbers and collagen content

Images of H&E-stained sections were used for this part of the analysis. The inbuilt QUPATH [80] algorithm for cell detection was used on manually selected regions of interest (mucosa, edema and muscularis externa). Picrosirius red-stained sections were analyzed using QUPATH. A machine-learning based algorithm was trained to detect collagen positive pixels and then run on the manually selected region of interest representing the three different tissue areas.

Pixel-by-pixel quantification of FnBPA5 versus total fibronectin intensity

FnBPA5 and fibronectin signals were analyzed using a pixel-by-pixel approach. For each mouse at least three different stitched 60× multi-tile images were used at different positions in the cecum and the z-stack maximum intensity projections were used to analyze the images. First, regions of interest in the three different tissue areas (mucosa, edema, muscularis externa) were annotated manually in IMAGEJ [81]. Second, all pixel values above the background channel noise were collected for a specific area. Data is represented as boxplots (from all the pixel values for each category) plus additionally randomly selected values (n = 100) as marker points indicating the distribution of pixel values left of the boxplots. FnBPA5 and control stainings with scrFnBPA5 were performed on neighboring sections for every mouse and the pixel-by-pixel analysis was performed identical for the FnBPA5- and scrFnBPA5-stained images. The gray bar represents the mean intensity (mean of various annotated image regions and mice) plus 3× standard deviation of the control marker scrFnBPA5 and serves as threshold above which FnBPA5 signal is considered specific.

Mass spectrometry sample preparation and processing

Laser Capture Microdissection was performed using the MMI CellCut Laser Capture Microdissection device (Molecular Machines & Industries, Eching, Germany). Twenty micrometer cryosections were captured on MMI membrane slides (MMI Prod. No. 50103) and subsequently stained with H&E using the MMI H&E Staining Kit Plus (MMI Prod. No. 70302). The microdissected tissue areas (in total 500 000 μm^2) were collected using mmi isolation cap tubes (200 µL) and kept at −20 °C until further processing. Sample lysis was performed directly on the tube lid. Tubes were opened upside down, fixed in this position and 10 µL RIPA buffer (25 mM Tris·HCl pH 7.6, 150 mM NaCl, 1% NP-40, 1% sodium deoxycholate, 0.1% SDS (Cat# 89900; Thermo Scientific)) were added onto the tissue on the lid. One microliter of 10× TCEP (Tris(2-carboxyethyl)phosphine hydrochloride, #C4706; Merck) was added to the lid and mixed carefully. One microliter of CAA (400 mM 2-Chloroacetamide, #C0267; Merck) was added, mixed carefully and the tubes were closed. The tissue was incubated for 30 min at room temperature. Liquid was spun down in a tabletop centrifuge and 48 µL ice-cold acetone 100% was added. Samples were incubated at −20 °C overnight. After acetone precipitation, the lids containing isolation caps were exchanged with normal lids to avoid detachment of the silicone inlets during high-speed centrifugation. Samples were centrifuged for 5 min at 21 000 ***g***. Then the acetone was removed, and the samples were air dried in fume hood. The samples were resuspended in 10 µL 4 M GdCl (Guanidinium Hydrochloride) in 50 mM HEPES (#G3272; Merck) and sonicated in a water bath sonicator for 10 min. For digestion the samples were diluted in 30 µL 50 mM HEPES (pH 8.5), LysC was added in a 1 : 50 ratio and samples were incubated for 4 h at 37 °C. Afterward, samples were diluted in another 30 µL 50 mM HEPES (pH 8.5), trypsin was added in a 1 : 10 protease : proteome ratio (w/w) and samples were incubated overnight at 37 °C at 350 r.p.m. Samples were then acidified with trifluoroacetic acid to a final concentration of 1% and pH was verified using pH strips. Subsequently, samples were centrifuged at 21 000 ***g*** for 15 min and transferred onto EvoTip Pure trap columns for desalting and loading the samples onto the LC–MS. The EvoTip Pure tips were used according to the manufacturer's instructions. In brief, Evotips were rinsed with 20 µL Solvent B (centrifugation at 800 ***g*** for 60 s). Then they were soaked in propanol until the Evotips turned pale white and equilibrated by soaking in 20 µL Solvent A (centrifugation at 800 ***g*** for 60 s). After loading the samples on the wet Evotips, they were

centrifuged again at 800 ***g*** for 60 s and washed with 20 µL Solvent A (centrifuged at 800 ***g*** for 60 s). Then, 100 µL Solvent A was added and the Evotips were centrifuged again at 800 ***g*** for 10 s only.

Data-independent acquisition mass spectrometry analysis

Samples were placed on the EvoSep One liquid chromatography system (EvoSep, Odense, Denmark) and analyzed inline with an Orbitrap Exploris 480 mass spectrometer (Thermo Fisher Scientific) coupled to a FAIMSpro device. Peptides were loaded on a EV1106 C18 column (15 cm × 150 µm, 1.9 µm diameter) and separated with the Whisper100 nanoflow and a 20SPD (samples per day) method consisting of a 58 min gradient. Eluting peptides were injected to the mass spectrometer using a 20 µm fused silica emitter (EV1087), at a static voltage of 2300 V, carrier gas flow of 3.6 $L \cdot min^{-1}$ and 240 °C ion transfer tube temperature and a positive polarity. A single compensation voltage of −45 V was applied to the FAIMS device during acquisition with a high-resolution MS1 (HRMS1) data-independent acquisition method. MS1 scans were recorded in the orbitrap detector at a 120 000 resolution, with a scan range of 400–1000 m/z, normalized AGC target of 300%, and injection time set to automatic. MS2 scans were recorded over the full m/z range with an isolation window of 8 m/z and 1 m/z window overlap. Peptides were fragmented using HCD (high collision dissociation), with a fixed normalized collision energy of 32%. The orbitrap resolution was set to 60 000 with first mass of 200 m/z. Normalized AGC target was set to 1000%, with maximum injection time set to automatic. MS1 scans were interspersed every 24 scan events (loop count 24), splitting the m/z range in three equal, 200 m/z parts. Raw data were searched with DIA-NN version 1.8, using a library-free (directDIA) approach and MS1 level quantification. The reference proteome was the mouse proteome database obtained from Uniprot (UP000000589 reviewed, accessed 17/06/2022). Precursor FDR was set to 1%, while Met N-terminal excision, Met oxidation and C carbamidomethylation were added as modifications. Match between runs and RT-dependent cross-run normalization were set to True. Trypsin/P was used as the protease, with one allowed missed cleavage, with otherwise default settings. Search results and protein quantification tables were used for further post-processing and analysis.

Acknowledgements

We thank Maike Wennekers Nielsen and Marie Vestergaard Lukassen at DTU for their technical support as well as Till Wüstemann for technical support at ETH Zurich. We thank Gianna La Regina and Stefanie Oswald for their great help during their semester projects. We also thank Valdemaras Petrosius and Erwin Schoof for mass spectrometry guidance and optimization of the in-house HRMS1 method. We gratefully acknowledge the Scientific Center for Optical and Electron Microscopy (ScopeM) of ETH Zurich, the ETH Phenomics center, and the Proteomics Core Facility at DTU for their support. This work was funded by NCCR Microbiomes, a research consortium financed by the Swiss National Science Foundation (ES); Swiss National Science Foundation (40B2-0_180953, 310030_185128) (ES) and (310030_204345), European Research Council Consolidator Grant (NUMBER 865730-SNUGly) (ES), Basel Research Centre for Child Health Multi-Invesitigator Project 2020 (BRCCH_MIP: Microbiota Engineering for Child Health) (ES, VV, RR). RR additionally was supported by the EMBO Scientific Exchange Grant (#9683). UK and KK are supported by a Novo Nordisk Foundation Young Investigator Award (NNF16OC0020670) and acknowledge funding from PRO-MS: Danish National Mass Spectrometry Platform for Functional Proteomics (grant no. 5072-00007B). The funders had no role in study design, data collection and analysis, decision to publish, or preparation of the manuscript. Open access funding provided by Eidgenossische Technische Hochschule Zurich.

Conflict of interest

VV is co-founder and scientific advisory board member of Tandem Therapeutics AG (CHE-192.070.977), an early-state start-up aiming to develop extracellular matrix targeting drugs. All other authors declare no conflict of interest.

Authors contributions

RR, VV, and ES contributed to study composition and design; RR and KK contributed to data collection; UK and KK contributed to analysis tools and expertise for the proteomics part; RR, VV, and ES contributed to draft manuscript preparation. All authors provided critical feedback to the manuscript. Tragically in August 2023, Prof. Ulrich auf dem Keller passed away. The responsibility for mass spectrometry data in this paper has been taken over by KK. The authors would like to dedicate this paper to Ulrich's memory. Without his brilliant scientific and technical insight and his enormous enthusiasm to explore new frontiers in science, this work would never have come about.

Peer review

The peer review history for this article is available at https://www.webofscience.com/api/gateway/wos/peer-review/10.1111/febs.17120.

Data availability statement

The mass spectrometry proteomics data have been deposited to the ProteomeXchange Consortium via the PRIDE [82] partner repository with the dataset identifier PXD043256. Materials available on request to the corresponding author.

References

1 Erben U, Loddenkemper C, Doerfel K, Spieckermann S, Haller D, Heimesaat MM, Zeitz M, Siegmund B & Kühl AA (2014) A guide to histomorphological evaluation of intestinal inflammation in mouse models. *Int J Clin Exp Pathol* **7**, 4557–4576.

2 Moore-Olufemi SD, Xue H, Attuwaybi BO, Fischer U, Harari Y, Oliver DH, Weisbrodt N, Allen SJ, Moore FA, Stewart R *et al.* (2005) Resuscitation-induced gut edema and intestinal dysfunction. *J Trauma* **58**, 264–270.

3 Uray KS, Laine GA, Xue H, Allen SJ & Cox CS (2006) Intestinal edema decreases intestinal contractile activity via decreased myosin light chain phosphorylation. *Crit Care Med* **34**, 2630–2637.

4 Moore-Olufemi SD, Padalecki J, Olufemi SE, Xue H, Oliver DH, Radhakrishnan RS, Allen SJ, Moore FA, Stewart R, Laine GA *et al.* (2009) Intestinal edema: effect of enteral feeding on motility and gene expression. *J Surg Res* **155**, 283–292.

5 World Health Organization (2018) Fact sheets – *Salmonella* (non-typhoidal).

6 Gong B, Li H, Feng Y, Zeng S, Zhuo Z, Luo J, Chen X & Li X (2022) Prevalence, serotype distribution and antimicrobial resistance of non-typhoidal *Salmonella* in hospitalized patients in Conghua District of Guangzhou, China. *Front Cell Infect Microbiol* **12**, 805384.

7 Majowicz SE, Musto J, Scallan E, Angulo FJ, Kirk M, O'Brien SJ, Jones TF, Fazil A, Hoekstra RM & International Collaboration on Enteric Disease 'Burden of Illness' Studies (2010) The global burden of nontyphoidal *Salmonella* gastroenteritis. *Clin Infect Dis* **50**, 882–889.

8 Hausmann A & Hardt W-D (2019) The interplay between *Salmonella enterica* serovar typhimurium and the intestinal mucosa during oral infection. *Microbiol Spectr* **7**, 41–57.

9 Wotzka SY, Nguyen BD & Hardt W-D (2017) *Salmonella* Typhimurium diarrhea reveals basic principles of enteropathogen infection and disease-promoted DNA exchange. *Cell Host Microbe* **21**, 443–454.

10 Barthel M, Hapfelmeier S, Quintanilla-Martínez L, Kremer M, Rohde M, Hogardt M, Pfeffer K, Rüssmann H & Hardt W-D (2003) Pretreatment of mice with streptomycin provides a *Salmonella enterica* serovar Typhimurium colitis model that allows analysis of both pathogen and host. *Infect Immun* **71**, 2839–2858.

11 Stecher B, Macpherson AJ, Hapfelmeier S, Kremer M, Stallmach T & Hardt W-D (2005) Comparison of *Salmonella enterica* serovar Typhimurium colitis in germfree mice and mice pretreated with streptomycin. *Infect Immun* **73**, 3228–3241.

12 Furter M, Sellin ME, Hansson GC & Hardt W-D (2019) Mucus architecture and near-surface swimming affect distinct *Salmonella* Typhimurium infection patterns along the murine intestinal tract. *Cell Rep* **27**, 2665–2678.e3.

13 Muniz LR, Knosp C & Yeretssian G (2012) Intestinal antimicrobial peptides during homeostasis, infection, and disease. *Front Immunol* **3**, 310.

14 Maier L, Diard M, Sellin ME, Chouffane E-S, Trautwein-Weidner K, Periaswamy B, Slack E, Dolowschiak T, Stecher B, Loverdo C *et al.* (2014) Granulocytes impose a tight bottleneck upon the gut luminal pathogen population during *Salmonella* Typhimurium colitis. *PLoS Pathog* **10**, e1004557.

15 Moor K, Diard M, Sellin ME, Felmy B, Wotzka SY, Toska A, Bakkeren E, Arnoldini M, Bansept F, Co AD *et al.* (2017) High-avidity IgA protects the intestine by enchaining growing bacteria. *Nature* **544**, 498–502.

16 Hausmann A, Böck D, Geiser P, Berthold DL, Fattinger SA, Furter M, Bouman JA, Barthel-Scherrer M, Lang CM, Bakkeren E *et al.* (2020) Intestinal epithelial NAIP/NLRC4 restricts systemic dissemination of the adapted pathogen *Salmonella* Typhimurium due to site-specific bacterial PAMP expression. *Mucosal Immunol* **13**, 530–544.

17 Fattinger SA, Geiser P, Ventayol PS, Martino MLD, Furter M, Felmy B, Bakkeren E, Hausmann A, Barthel-Scherrer M, Gül E *et al.* (2021) Epithelium-autonomous NAIP/NLRC4 prevents TNF-driven inflammatory destruction of the gut epithelial barrier in *Salmonella*-infected mice. *Mucosal Immunol* **14**, 615–629.

18 Stecher B, Robbiani R, Walker AW, Westendorf AM, Barthel M, Kremer M, Chaffron S, Macpherson AJ, Buer J, Parkhill J *et al.* (2007) *Salmonella enterica* serovar Typhimurium exploits inflammation to compete with the intestinal microbiota. *PLoS Biol* **5**, 2177–2189.

19 Stewart RH (2020) A modern view of the interstitial space in health and disease. *Front Vet Sci* **7**, 609583.
20 Pompili S, Latella G, Gaudio E, Sferra R & Vetuschi A (2021) The charming world of the extracellular matrix: a dynamic and protective network of the intestinal wall. *Front Med* **8**, 610189.
21 Theocharis AD, Manou D & Karamanos NK (2019) The extracellular matrix as a multitasking player in disease. *FEBS J* **286**, 2830–2869.
22 Hynes RO (2009) The extracellular matrix: not just pretty fibrils. *Science* **326**, 1216–1219.
23 Patten J & Wang K (2020) Fibronectin in development and wound healing. *Adv Drug Deliv Rev* **170**, 353–368.
24 Lenselink EA (2015) Role of fibronectin in normal wound healing. *Int Wound J* **12**, 313–316.
25 George EL, Georges-Labouesse EN, Patel-King RS, Rayburn H & Hynes RO (1993) Defects in mesoderm, neural tube and vascular development in mouse embryos lacking fibronectin. *Development* **119**, 1079–1091.
26 Vogel V (2018) Unraveling the mechanobiology of extracellular matrix. *Annu Rev Physiol* **80**, 353–387.
27 Ortiz Franyuti D, Mitsi M & Vogel V (2017) Mechanical stretching of fibronectin fibers upregulates binding of interleukin-7. *Nano Lett* **18**, 15–25.
28 Selcuk K, Leitner A, Braun L, Blanc FL, Pacak P, Pot S & Vogel V (2023) Tissue transglutaminase 2 has higher affinity for relaxed than for stretched fibronectin fibers. *Matrix Biol* **125**, 113–132.
29 Kubow KE, Vukmirovic R, Zhe L, Klotzsch E, Smith ML, Gourdon D, Luna S & Vogel V (2015) Mechanical forces regulate the interactions of fibronectin and collagen I in extracellular matrix. *Nat Commun* **6**, 8026.
30 Smith ML, Gourdon D, Little WC, Kubow KE, Eguiluz RA, Luna-Morris S & Vogel V (2007) Force-induced unfolding of fibronectin in the extracellular matrix of living cells. *PLoS Biol* **5**, e268.
31 Li B, Moshfegh C, Lin Z, Albuschies J & Vogel V (2013) Mesenchymal stem cells exploit extracellular matrix as mechanotransducer. *Sci Rep* **3**, 2425.
32 Baneyx G, Baugh L & Vogel V (2001) Coexisting conformations of fibronectin in cell culture imaged using fluorescence resonance energy transfer. *Proc Natl Acad Sci USA* **98**, 14464–14468.
33 Hertig S, Chabria M & Vogel V (2012) Engineering mechanosensitive multivalent receptor–ligand interactions: why the nanolinker regions of bacterial adhesins matter. *Nano Lett* **12**, 5162–5168.
34 Meenan NAG, Visai L, Valtulina V, Schwarz-Linek U, Norris NC, Gurusiddappa S, Höök M, Speziale P & Potts JR (2007) The tandem β-zipper model defines high affinity fibronectin-binding repeats within *Staphylococcus aureus* FnBPA. *J Biol Chem* **282**, 25893–25902.
35 Chabria M, Hertig S, Smith ML & Vogel V (2010) Stretching fibronectin fibres disrupts binding of bacterial adhesins by physically destroying an epitope. *Nat Commun* **1**, 135.
36 Fonta CM, Arnoldini S, Jaramillo D, Moscaroli A, Oxenius A, Behe M & Vogel V (2020) Fibronectin fibers are highly tensed in healthy organs in contrast to tumors and virus-infected lymph nodes. *Matrix Biol Plus* **8**, 100046.
37 Arnoldini S, Moscaroli A, Chabria M, Hilbert M, Hertig S, Schibli R, Béhé M & Vogel V (2017) Novel peptide probes to assess the tensional state of fibronectin fibers in cancer. *Nat Commun* **8**, 1793.
38 Fonta CM, Loustau T, Li C, Surendran SP, Hansen U, Murdamoothoo D, Benn MC, Velazquez-Quesada I, Carapito R, Orend G *et al.* (2023) Infiltrating CD8+ T cells and M2 macrophages are retained in tumor matrix tracks enriched in low tension fibronectin fibers. *Matrix Biol* **116**, 1–27.
39 Maier L, Vyas R, Cordova CD, Lindsay H, Schmidt TSB, Brugiroux S, Periaswamy B, Bauer R, Sturm A, Schreiber F *et al.* (2013) Microbiota-derived hydrogen fuels *Salmonella* Typhimurium invasion of the gut ecosystem. *Cell Host Microbe* **14**, 641–651.
40 Nguyen BD, Cuenca M, Hartl J, Gül E, Bauer R, Meile S, Rüthi J, Margot C, Heeb L, Besser F *et al.* (2020) Import of aspartate and malate by DcuABC drives H2/fumarate respiration to promote initial *Salmonella* gut-lumen colonization in mice. *Cell Host Microbe* **27**, 922–936.e6.
41 Diller RB & Tabor AJ (2022) The role of the extracellular matrix (ECM) in wound healing: a review. *Biomimetics* **7**, 87.
42 Hwang J, Huang Y, Burwell TJ, Peterson NC, Connor J, Weiss SJ, Yu SM & Li Y (2017) In situ imaging of tissue remodeling with collagen hybridizing peptides. *ACS Nano* **11**, 9825–9835.
43 Li Y & Yu SM (2013) Targeting and mimicking collagens via triple helical peptide assembly. *Curr Opin Chem Biol* **17**, 968–975.
44 Klotzsch E, Smith ML, Kubow KE, Muntwyler S, Little WC, Beyeler F, Gourdon D, Nelson BJ & Vogel V (2009) Fibronectin forms the most extensible biological fibers displaying switchable force-exposed cryptic binding sites. *Proc Natl Acad Sci USA* **106**, 18267–18272.
45 Wiig H, Rubin K & Reed RK (2003) New and active role of the interstitium in control of interstitial fluid pressure: potential therapeutic consequences. *Acta Anaesthesiol Scand* **47**, 111–121.
46 Reed RK & Rubin K (2010) Transcapillary exchange: role and importance of the interstitial fluid pressure and the extracellular matrix. *Cardiovasc Res* **87**, 211–217.

47 Reed RK, Lidén Å & Rubin K (2010) Edema and fluid dynamics in connective tissue remodelling. *J Mol Cell Cardiol* **48**, 518–523.
48 Zollinger AJ & Smith ML (2017) Fibronectin, the extracellular glue. *Matrix Biol* **60**, 27–37.
49 Xuan Y, Bateman NW, Gallien S, Goetze S, Zhou Y, Navarro P, Hu M, Parikh N, Hood BL, Conrads KA *et al*. (2020) Standardization and harmonization of distributed multi-center proteotype analysis supporting precision medicine studies. *Nat Commun* **11**, 5248.
50 Demichev V, Messner CB, Vernardis SI, Lilley KS & Ralser M (2020) DIA-NN: neural networks and interference correction enable deep proteome coverage in high throughput. *Nat Methods* **17**, 41–44.
51 Zhou Y, Zhou B, Pache L, Chang M, Khodabakhshi AH, Tanaseichuk O, Benner C & Chanda SK (2019) Metascape provides a biologist-oriented resource for the analysis of systems-level datasets. *Nat Commun* **10**, 1523.
52 Naba A, Pearce OMT, Rosario AD, Ma D, Ding H, Rajeeve V, Cutillas PR, Balkwill FR & Hynes RO (2017) Characterization of the extracellular matrix of normal and diseased tissues using proteomics. *J Proteome Res* **16**, 3083–3091.
53 Silverman GA, Bird PI, Carrell RW, Church FC, Coughlin PB, Gettins PGW, Irving JA, Lomas DA, Luke CJ, Moyer RW *et al*. (2001) The serpins are an expanding superfamily of structurally similar but functionally diverse proteins. *J Biol Chem* **276**, 33293–33296.
54 Bao J, Pan G, Poncz M, Wei J, Ran M & Zhou Z (2018) Serpin functions in host-pathogen interactions. *PeerJ* **6**, e4557.
55 Johannes L, Jacob R & Leffler H (2018) Galectins at a glance. *J Cell Sci* **131**, jcs208884.
56 Liu F-T & Stowell SR (2023) The role of galectins in immunity and infection. *Nat Rev Immunol* **23**, 479–494.
57 Xia C, Braunstein Z, Toomey AC, Zhong J & Rao X (2018) S100 proteins as an important regulator of macrophage inflammation. *Front Immunol* **8**, 1908.
58 McQuitty CE, Williams R, Chokshi S & Urbani L (2020) Immunomodulatory role of the extracellular matrix within the liver disease microenvironment. *Front Immunol* **11**, 574276.
59 Potekaev NN, Borzykh OB, Medvedev GV, Pushkin DV, Petrova MM, Petrov AV, Dmitrenko DV, Karpova EI, Demina OM & Shnayder NA (2021) The role of extracellular matrix in skin wound healing. *J Clin Med* **10**, 5947.
60 Pfisterer K, Shaw LE, Symmank D & Weninger W (2021) The extracellular matrix in skin inflammation and infection. *Front Cell Dev Biol* **9**, 682414.
61 Seltana A, Cloutier G, Nicolas VR, Khalfaoui T, Teller IC, Perreault N & Beaulieu J-F (2022) Fibrin(ogen) is constitutively expressed by differentiated intestinal epithelial cells and mediates wound healing. *Front Immunol* **13**, 916187.
62 Thomas PD, Ebert D, Muruganujan A, Mushayahama T, Albou L & Mi H (2022) PANTHER: making genome-scale phylogenetics accessible to all. *Protein Sci* **31**, 8–22.
63 Mi H & Thomas P (2009) Protein networks and pathway analysis. *Methods Mol Biol* **563**, 123–140.
64 Rawlings ND, Waller M, Barrett AJ & Bateman A (2014) MEROPS: the database of proteolytic enzymes, their substrates and inhibitors. *Nucleic Acids Res* **42**, D503–D509.
65 Morita Y, Araki H, Sugimoto T, Takeuchi K, Yamane T, Maeda T, Yamamoto Y, Nishi K, Asano M, Shirahama-Noda K *et al*. (2007) Legumain/asparaginyl endopeptidase controls extracellular matrix remodeling through the degradation of fibronectin in mouse renal proximal tubular cells. *FEBS Lett* **581**, 1417–1424.
66 Dourdin N, Brustis J-J, Balcerzak D, Elamrani N, Poussard S, Cottin P & Ducastaing A (1997) Myoblast fusion requires fibronectin degradation by exteriorized m-calpain. *Exp Cell Res* **235**, 385–394.
67 Wan F, Letavernier E, Abid S, Houssaini A, Czibik G, Marcos E, Rideau D, Parpaleix A, Lipskaia L, Amsellem V *et al*. (2016) Extracellular calpain/calpastatin balance is involved in the progression of pulmonary hypertension. *Am J Respir Cell Mol Biol* **55**, 337–351.
68 Hennig GW, Costa M, Chen BN & Brookes SJH (1999) Quantitative analysis of peristalsis in the Guinea-pig small intestine using spatio-temporal maps. *J Physiol* **517**, 575–590.
69 Gayer CP & Basson MD (2009) The effects of mechanical forces on intestinal physiology and pathology. *Cell Signal* **21**, 1237–1244.
70 Swartz MA & Lund AW (2012) Lymphatic and interstitial flow in the tumour microenvironment: linking mechanobiology with immunity. *Nat Rev Cancer* **12**, 210–219.
71 Malijauskaite S, Connolly S, Newport D & McGourty K (2021) Gradients in the in vivo intestinal stem cell compartment and their in vitro recapitulation in mimetic platforms. *Cytokine Growth Factor Rev* **60**, 76–88.
72 Du H, Bartleson JM, Butenko S, Alonso V, Liu WF, Winer DA & Butte MJ (2023) Tuning immunity through tissue mechanotransduction. *Nat Rev Immunol* **23**, 174–188.
73 Roy M-F & Malo D (2002) Genetic regulation of host responses to *Salmonella* infection in mice. *Genes Immun* **3**, 381–393.
74 Oberhauser AF, Badilla-Fernandez C, Carrion-Vazquez M & Fernandez JM (2002) The mechanical hierarchies of fibronectin observed with single-molecule AFM. *J Mol Biol* **319**, 433–447.

75 Little WC, Schwartlander R, Smith ML, Gourdon D & Vogel V (2009) Stretched extracellular matrix proteins turn fouling and are functionally rescued by the chaperones albumin and casein. *Nano Lett* **9**, 4158–4167.
76 Baneyx G, Baugh L & Vogel V (2002) Fibronectin extension and unfolding within cell matrix fibrils controlled by cytoskeletal tension. *Proc Natl Acad Sci USA* **99**, 5139–5143.
77 Nikolaev M, Mitrofanova O, Broguiere N, Geraldo S, Dutta D, Tabata Y, Elci B, Brandenberg N, Kolotuev I, Gjorevski N *et al.* (2020) Homeostatic mini-intestines through scaffold-guided organoid morphogenesis. *Nature* **585**, 574–578.
78 Taelman J, Diaz M & Guiu J (2022) Human intestinal organoids: promise and challenge. *Front Cell Dev Biol* **10**, 854740.
79 3Helix (2019) User guide for research use only product number specialty molecular features of CHP reagents.
80 Bankhead P, Loughrey MB, Fernández JA, Dombrowski Y, McArt DG, Dunne PD, McQuaid S, Gray RT, Murray LJ, Coleman HG *et al.* (2017) QuPath: open source software for digital pathology image analysis. *Sci Rep* **7**, 16878.
81 Schneider CA, Rasband WS & Eliceiri KW (2012) NIH Image to ImageJ: 25 years of image analysis. *Nat Methods* **9**, 671–675.
82 Perez-Riverol Y, Bai J, Bandla C, García-Seisdedos D, Hewapathirana S, Kamatchinathan S, Kundu DJ, Prakash A, Frericks-Zipper A, Eisenacher M *et al.* (2021) The PRIDE database resources in 2022: a hub for mass spectrometry-based proteomics evidences. *Nucleic Acids Res* **50**, D543–D552.

Supporting information

Additional supporting information may be found online in the Supporting Information section at the end of the article.

Fig. S1. Overview of H&E-stained cecal cryosections of *S.* Tm and mock infected C57BL/6 mice shows decrease in overall cecum size and changes in tissue morphology.

Video S1. Video through z-stack of collagen hybridizing peptide-stained edema (24 h p.i.) reveals damaged collagens.

Video S2. Video through z-stack of collagen hybridizing peptide-stained edema (48 h p.i.) reveals damaged collagens.

Video S3. Video through z-stack of fibronectin network in edema (24 h p.i.) reveals cells intermingled with fibronectin fibers.

Video S4. Video through z-stack of fibronectin network in edema (48 h p.i.) reveals cells intermingled with fibronectin fibers.